



## Illuminating the near-sonic rupture velocities of the intracontinental Kokoxili $M_w$ 7.8 and Denali fault $M_w$ 7.9 strike-slip earthquakes with global P wave back projection imaging

Kristoffer T. Walker<sup>1</sup> and Peter M. Shearer<sup>1</sup>

Received 6 April 2008; revised 26 August 2008; accepted 14 October 2008; published 13 February 2009.

[1] The Denali and Kokoxili strike-slip earthquakes are two of the longest recent intracontinental ruptures. Previous studies report a range of rupture velocities. Here we image these earthquakes by reverse time migration of the intermediate-frequency P wave train recorded by global broadband seismometers. This technique permits a relatively direct measure of rupture velocity (speed and direction) as constrained by the radiated seismic energy, free from restrictive assumptions or rupture speed bounds placed on the solution. We compare our results with published seismic, GPS displacement, and surface slip inversion results. Both ruptures were initially subshear and transitioned over a distance no longer than 40 km to supershear speeds close to the P wave speed of  $\sim 5.6$  km/s. We investigate the accuracy of our results with synthetic data and experiment with using different imaging parameters and seismic subnetworks. These tests allow us to rule out the possibility of subshear speeds along the supershear segments. Although we cannot exclude supershear speeds of 4.5–6.5 km/s, our most reliable rupture velocities of  $\sim 5.6$  km/s are close to the local P wave speeds. We hypothesize that these intracontinental faults have weak shear strengths or high breakdown slips or crustal rigidities and experience at least moderate slip or slip rate weakening. Our observations and previous published results lead us to speculate that very long, surface-extending faults with general homogeneity in prestress and fault strength, together with smaller adjacent fault segments to provide triggering, may be necessary ingredients for the sub-Rayleigh to supershear rupture speed transition in strike-slip earthquakes.

**Citation:** Walker, K. T., and P. M. Shearer (2009), Illuminating the near-sonic rupture velocities of the intracontinental Kokoxili  $M_w$  7.8 and Denali fault  $M_w$  7.9 strike-slip earthquakes with global P wave back projection imaging, *J. Geophys. Res.*, *114*, B02304, doi:10.1029/2008JB005738.

### 1. Introduction

[2] On 14 November 2001, the  $M_w$  7.8 Kokoxili (Kunlunshan) earthquake ruptured the Kunlun strike-slip fault in northern Tibet. Twelve months later, on 3 November 2002, the  $M_w$  7.9 Denali fault earthquake ruptured the Denali and Totschunda strike-slip faults in Alaska. Both ruptures initiated on a secondary fault, ruptured toward the east for at least 300 km, and were well recorded at teleseismic distances, providing two similar events with which to investigate the kinematics and dynamics of the rupture process of very long strike-slip earthquakes.

[3] One of the important quantities in understanding the physics of these long ruptures and the hazards they present to society is the speed with which the rupture front propagates [e.g., Das, 2007]. Strike-slip ruptures are thought to be akin to movement of a mode II crack, in

which the rupture direction coincides with the slip direction on one side of the fault. Theoretical results predict that the rupture is allowed to propagate within two steady state speed regimes: below Rayleigh wave speed (subshear) or between the S and P wave speeds (supershear). Burridge [1973] and Andrews [1976] proposed the “BAM model,” which explains how a subshear rupture can transition to supershear. As a subshear crack propagates, a peak in shear stress traveling at the S wave speed can develop ahead of the crack tip such that if the peak in stress is above a critical threshold and the fault is longer than a critical length, supershear can initiate. Otherwise, simple rupture at sub-Rayleigh wave speeds will occur. This model has been supported and expanded upon [e.g., Das and Aki, 1977]. Technological advancements in computers and fracture mechanics experimentation techniques have permitted further investigation of the transition phenomenon [Day, 1982; Rosakis et al., 1999; Madariaga and Olsen, 2000; Rosakis, 2002; Dunham et al., 2003; Xia et al., 2004; Dunham, 2007].

[4] Supershear rupture speeds have been reported for the Denali and Kokoxili earthquakes [e.g., Bouchon and Vallée, 2003; Frankel, 2004; Antolik et al., 2004; Dunham and Archuleta, 2004; Robinson et al., 2006; Vallée et al., 2008].

<sup>1</sup>Institute of Geophysics and Planetary Physics, Scripps Institution of Oceanography, University of California, San Diego, La Jolla, California, USA.

However, other studies have obtained subshear rupture speeds for the same events [e.g., *Dreger et al.*, 2004; *Ozacar and Beck*, 2004; *Olson et al.*, 2003; *Shao and Ji*, 2007; *Liao and Huang*, 2008]. These discrepancies may be due to the analysis of different frequency bands, incorrect assumptions inherent in the techniques employed, nonuniqueness of the inversions, resolution limitations, or rupture complexity.

[5] In order to understand the physical processes involved in these very long ruptures and to relate them to recent modeling studies, the rupture speeds must be constrained better in space and time. Here, we show that the teleseismic P wave train of these earthquakes can be reverse time migrated to unambiguously illuminate the rupture speed and direction along most of the rupture. We find that both earthquakes began as subshear ruptures but at about 100 km into the rupture clearly transitioned to supershear speeds near the local P wave speed, over a transition distance no longer than 40 km, and continued for at least another 200 km. To first order, these results are consistent with those of *Robinson et al.* [2006] and *Vallée et al.* [2008] for the Kokoxili rupture. For the Denali rupture, our results extend the localized constraints on supershear speeds of *Dunham and Archuleta* [2004] and *Frankel* [2004] to the end of the rupture. Both ruptures are remarkably similar despite the ruptured fault segments' different geologic ages and geometries. We compare our results to those obtained with other techniques, and make inferences about the dynamics of the rupture process for the Denali and Kokoxili earthquakes.

## 2. Tectonic Setting

### 2.1. Kunlun Fault, Northern Tibetan Plateau

[6] The left-lateral Kunlun fault separates the high Tibetan Plateau to the south from the sedimentary basins to the north. Just south of the Kunlun Mountains, this Miocene fault extends east/west for about 1600 km, accommodating about 10–12 mm/a of eastward motion of the Tibetan Plateau (with respect to the basins in the north) for a total horizontal offset of less than 100 km (about a third to a half of the total motion [*Peltzer and Saucier*, 1996; *Van der Woerd et al.*, 1998, 2000, 2002]). The Qaidam Basin underthrusts the Kunlun Mountains, accommodating about half of the north/south convergence between the Indian subcontinent and Eurasia [*Meyer et al.*, 1998; *Tapponnier et al.*, 2001].

[7] The Tibetan Plateau has a crustal thickness that is twice the thickness of normal continental crust [e.g., *Chun and Yoshii*, 1977; *Hirn et al.*, 1984]. Hydrothermal activity, which may be associated with high crustal pore fluid pressures and weak fault planes, is abundant at the surface, with numerous lakes and streams that border the Kunlun fault. Anomalies in seismic reflection [*Makovsky et al.*, 1996; *Makovsky and Klempner*, 1999], converted P-to-S waves [*Kind et al.*, 1996], and magnetotelluric data [*Chen et al.*, 1996] suggest at ~15 km depth the presence of aqueous fluids [*Makovsky and Klempner*, 1999]. Alternatively, these anomalies have been interpreted to represent a partially molten layer [*Nelson et al.*, 1996].

### 2.2. Denali Fault System, South Central Alaska

[8] The 2000-km-long Denali fault is part of a series of parallel faults that accommodate right-lateral to oblique

convergence between the North American and Pacific plates. The Denali fault separates the Wrangellia, southern margin, and Yakutat terranes to the south from the Alaska margin to the north [*Plafker and Berg*, 1994]. The Wrangellia terrane was accreted to the Alaska margin during the middle Cretaceous. The subsequent counterclockwise rotation of Alaska due to the opening of the Canada basin and a more northerly Pacific plate motion led to right-lateral slip along the Denali fault. This slip rate intensified during the early Tertiary when compression between the Eurasian and North American plates led to further counterclockwise rotation and a space problem for northward moving terranes in southeast Alaska [*Plafker and Berg*, 1994]. Since the Oligocene, right-lateral strike slip continued along the Denali fault with a Holocene slip rate of ~15 mm/a and a total horizontal offset of ~400 km [*Lanphere*, 1978; *Nokleberg et al.*, 1994; *Plafker et al.*, 1994].

[9] The top of the subducted Pacific plate is located between 80 and 100 km depth beneath the western Denali fault system [*Ferris et al.*, 2003]. The slab does not exist beneath the eastern end of the fault. The Denali fault also demarks a 10 to 15 km step in crustal thickness, with a thickness of 40–45 km to the south, and 30 km to the north [e.g., *Brocher et al.*, 2004; *Rossi et al.*, 2006]. Because of the extensive history of slip and deformation, the Denali fault juxtaposes different rock units along the strike of the fault, but most units are either metasedimentary or metaigneous rocks. There are also a number of glaciers located along the fault to the east of the Totschunda fault, and hydrothermal activity in the region is associated with fractured, granitic plutons [*Miller*, 1994].

### 2.3. Seismic Modeling and Imaging

[10] Two seismic approaches to investigating the rupture dynamics of earthquakes are inverse modeling of waveforms and imaging. A variety of waveform modeling techniques can provide an estimate of the spatiotemporal slip distribution. Most of these techniques require a priori knowledge of at least some fault parameters and the calculation of Green's functions between points along the assumed fault plane and the stations. An inversion is performed with stability constraints to minimize the difference between predicted and observed seismograms. Some issues with these techniques are discussed by *Beresnev* [2003]. For large earthquakes, arguably the biggest issue is that there are many model solutions that fit the data well and inversion results among different groups exhibit only limited agreement.

[11] There are a number of seismic reflection imaging techniques that have been advanced by the seismic exploration community over the last 20 years. These techniques rely on phase coherence in order to reverse time migrate (or back project) the energy recorded by geophones to impedance contrasts (geologic interfaces) at depth, which is especially important for eliminating diffractions that make distinguishing the edges of impedance contrasts difficult. Reverse time migration, hereinafter referred to as "back projection," is one of these techniques and does not require many assumptions. Although there are many back projection implementations [e.g., *Claerbout*, 1971; *Stolt*, 1978; *McMechan*, 1983; *Baysal et al.*, 1983; *Bleistein*, 1987; *Sun et al.*, 2000], the physical concept is the same and can be

applied to imaging the seismic energy that is radiated during an earthquake rupture.

[12] *Ishii et al.* [2005, 2007] used the Japanese High-Sensitivity Seismograph Network (Hi-net) array to image the rupture extent, direction, and velocity of the Sumatra-Andaman  $M_w$  9.2 2004 earthquake. They used short-period records from the bottom of 100 m boreholes in the Japanese Hi-net array, and back projected high-frequency, phase-coherent energy to the source location  $\sim 50^\circ$  away. The success of the technique was due to the phase coherence across the array, which was a result of the high quality of the recorded direct P waves, the favorable source-to-station geometry, and the relatively small along-rupture changes in the velocity structure to the stations. *Walker et al.* [2005] used a similar approach with 0.03–0.5 Hz waveforms recorded by global seismic stations to image the rupture details of the Sumatra 2005  $M_w$  8.6 earthquake. They used a station-weighting scheme that effectively regularized their uneven station distribution. Comparisons with the results from the Hi-net array suggested that, for this earthquake, the global network produced less smearing artifacts and a sharper image. In contrast to the resolved unilateral rupture of the 2004  $M_w$  9.2 earthquake, the 2005  $M_w$  8.6 earthquake was bilateral, rupturing to the north and south. *Larmat et al.* [2006] used a reverse-time wave propagation method on the complete wavefield recorded by global seismic stations to image the 2004 Sumatra earthquake. Their synthetic seismogram approach naturally took into account many of the complexities of the different phases and propagation paths, although the long periods of the Rayleigh waves that dominated their solution limited the resolution they obtained at the source.

[13] A different approach was taken by *Krüger and Ohrnberger* [2005]. They used the European subnetwork as an array, a curved wavefront assumption, and beam formed a low-frequency band (0.03–0.05 Hz) of the P wave train of the 2004 Sumatra rupture to obtain back azimuth and slowness as a function of time using a European reference point. They then shot P rays in the directions determined by the beam forming, and tracked the intersection of those rays with the hypocentral depth to recover rupture details that were similar to those of *Ishii et al.* [2005]. A similar approach was taken by *Spudich and Cranswick* [1984] to image the rupture propagation of the 1979  $M_s$  6.9 Imperial Valley earthquake. They used a short baseline accelerometer array of five stations to image a super-shear rupture in the 1.5+ Hz frequency band along a 7-km-long segment of the  $\sim 35$ -km-long rupture. However, they could only reliably measure vertical slowness, which limited their ability to accurately track the rupture due to the unfavorable source array geometry. *Kao and Shan* [2004, 2007] applied a related technique that they refer to as “source scanning” to resolve the location of tremor in the Cascadia subduction zone and the ruptures of the San Simeon and Parkfield earthquakes. Their technique is different in that they back project envelope functions and absolute amplitudes using local seismic data. They back projected to a three-dimensional spatial grid that included depth as well as horizontal position. *Kao et al.* [2008] also used back projection with three-dimensional ray tracing to identify the rupture plane of the 2001 Nisqually, Washington, earthquake. Finally, *Allmann and Shearer* [2007]

implemented the back projection approach to image a secondary high-frequency event during the 2004 Parkfield earthquake. They back projected S waves recorded in local strong motion data to a spatial three-dimensional source grid. Although appropriate for local imaging, resolution with depth is relatively poor at teleseismic distances.

### 3. Methodology, Data Selection, and Processing

[14] The back projection methodology that we employ below is a modified version of that used by *Walker et al.* [2005]. We assume that the energy in the P wave train in the  $\sim 0.1$ –1.0 Hz band originates directly from the rupture, and we use a simple ray theoretical approach that only considers travel times (because we apply automatic gain control “AGC” to the data, we ignore geometrical spreading, directivity and other amplitude effects). A 3-D grid  $(x, y, t)$  of possible source points is defined at the hypocentral depth encompassing the source region (Figure 1). For each possible source point and time sample, a travel time curve is defined using the IASP91 velocity model [*Kennett and Engdahl*, 1991], along which the amplitudes are summed to form the stack  $S(x, y, t)$ , which is an estimate of the source time function for a source at the associated grid point. Space-time peaks in the  $S(x, y, t)$  function represent likely sources of seismic radiation, which, given sufficient resolution, can be used to map the rupture history of the event.

[15] Velocity heterogeneity along the raypaths between the source region and the stations accounts for time shift deviations of up to  $\sim 5$  s from the IASP91 predictions (Figure 1a). Therefore, a modified iterative cross-correlation analysis [*Houser et al.*, 2008] is used on the first several seconds of the P wave train to define a time shift correction (Figure 1b) and polarity correction (Figure 1c), which maximizes  $S(0,0,t)$  (at the hypocenter). Subevents with similar focal mechanisms to the first-motion mechanism also coherently stack at later times (Figure 1d). However, if the subevents have mechanisms that are significantly different than that of the first-motion mechanism,  $S(x, y, t)$  is attenuated unless specific subnetworks of the available stations carefully selected for use.

[16] We selected all available vertical component P wave trains that were archived by the IRIS Data Management Center. Velocity waveforms were selected for stations within  $30$ – $90^\circ$  from the epicenter, filtered, and resampled to 50 Hz. To improve phase coherence within the P wave train, a five-pole, zero-phase Butterworth band-pass filter was applied in the 0.2–0.9 Hz band for the Kokoxili rupture and 0.1–0.5 Hz band for the Denali rupture. These frequency bands were chosen on the basis of many resolution tests to find the optimum frequency band that maximized the imaging coherence. These filters also attenuated the lower-frequency surface reflections, such as PP, which does not arrive until after 70 s for the closest stations. The PP phase, as well as other phases like PcP, have different move out curves, and will not align along that for the direct P wave (Figure 1). Therefore, this misalignment along with the applied AGC makes their contribution to  $S(x, y, t)$  extremely small.

[17] The cross-correlation analysis used a subset of the stations as defined by a signal-to-noise ratio (SNR) threshold of 12 dB. The resolution of the back projection

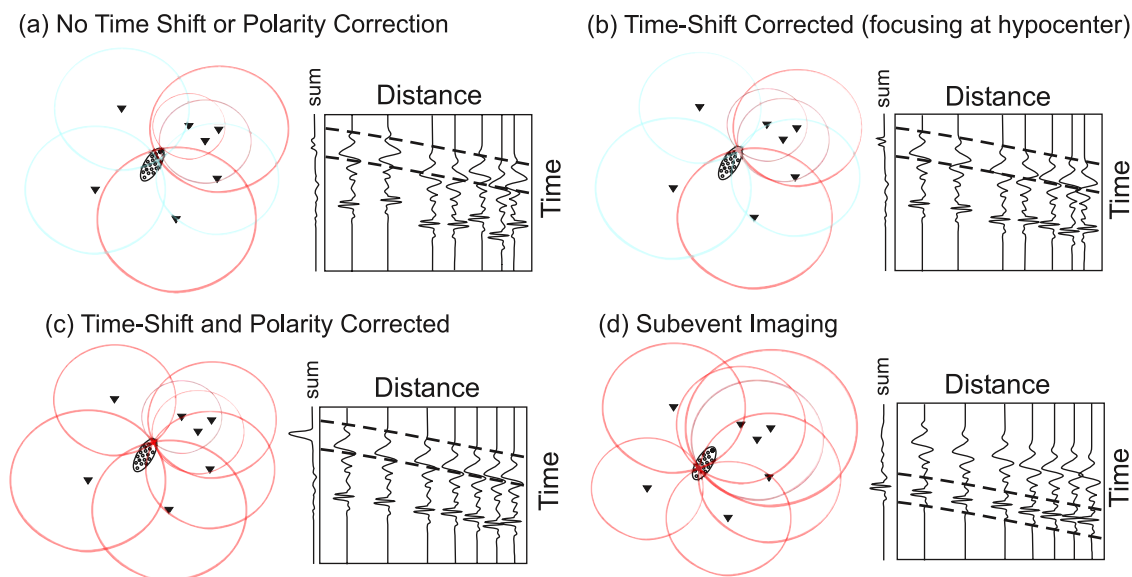


**Figure 1.** Schematic showing the back projection method applied to imaging earthquake ruptures. The rupture is approximated by a horizontal grid of source points at the hypocentral depth. The P waves recorded at the seismic stations (triangles) are projected backward in time, interfering constructively at locations where the seismic energy originated, after time shift (3-D velocity heterogeneity) and polarity (focal mechanism) corrections have been made. Subevents at different locations from the hypocenter can also be resolved.

approach depends upon many factors including the frequency content of the data and the network geometry. We have found that better results are generally obtained for more uniform station distributions and thus we apply the station-weighting scheme used by *Walker et al.* [2005] to even out the station distribution and prevent a large density of stations in a single region from dominating the solution. For the cross correlation, the weight of each station is  $1/n$ , where  $n$  is the number of stations within 300 km. We apply an STA/LTA autopicker [Earle and Shearer, 1994] to pick the first arrival at each station and use the median of the residual between the picks and the IASP91 predicted times as the initial reference time. The signal window was between  $-3$  and  $6$  s and was allowed to shift by up to  $\pm 6$  s. The algorithm loops over the starting station, performing five iterations for each trial alignment and calculating the average correlation coefficient  $r_{avg}$ . The optimum alignment is that associated with the starting station that yields the best  $r_{avg}$ .

[18] The final master stack, a proxy for the source time function at the hypocenter, has the best SNR of all the traces. To correct for the radially symmetric velocity model (or any potential inaccuracy in the origin time of the earthquake), we apply the autopicker to the master stack to pick the onset of the rupture and provide an additional timing correction  $t_c$ . We also discard any traces for which the final shifts are greater than  $5$  s ( $t_{max}$ ) of the predicted arrival time (minus  $t_c$ ). The cross-correlation analysis also provides a polarity correction for each trace. These polarity corrections should be consistent with that predicted by first-motion focal mechanisms. We discuss later for each earthquake how we select a subnetwork of stations on the basis of the first-motion and CMT focal mechanisms so we can better image the rupture as it undergoes along-fault changes in the focal mechanism.

[19] Prior to back projection, we apply a time-variable gain (automatic gain control) to normalize the amplitudes using a 5-s time window, maximizing our ability to track the rupture velocity along the entire rupture. We only use waveforms for which the cross-correlation coefficient is greater than some threshold  $r_{min}$ . We also used the same station regularization scheme, but with different parameters ( $w_b$ ). These data are then back projected and the resulting stacks  $S(x, y, t)$  are decimated in time to a 3 Hz sampling rate. At its full time-space resolution, the resulting  $S(x, y, t)$  image contains numerous high-frequency and short-wavelength features that are not reliable measures of source properties. The back projection method involves the constructive and destructive interference of wavefronts from the different stations. The destructive interference of incoherent energy is never complete and obvious artifacts can sometimes be seen that sweep through the image at the apparent speeds of the direct teleseismic P phase of 14 to 22 km/s (i.e., the horizontal speed of the P arrivals at each station). To suppress these artifacts and focus on the highest amplitude and most reliable parts of the image, we apply a space-time smoothing operator to  $S(x, y, t)$ . We use a scaling speed of 3 km/s to convert time to pseudo-space, and integrate  $S(x, y, t)^2$  with a running cube operator of width  $d_c$ , resulting in  $S_i(x, y, t)^2$ . This operator preserves energy that travels through  $S(x, y, t)$  at slow speeds (such as the constructively interfering energy that delineates the rupture), but helps attenuate artifacts that sweep through at the faster apparent speeds of the direct P phase. We then search  $S_i(x, y, t)^2$  for energetic points that are defined as local maxima (in  $x, y, t$ ) that are greater than  $e_{min}$  of the global maximum. We then sort these local maxima by their amplitude. Starting from the maximum energy points and working down, we discard any points that are within a threshold distance  $d_e$  (using the

**Table 1.** Back Projection Imaging Parameters

	$r_{\min}$	$t_{\max}$ (s)	$w_b$ (km)	$r_{\text{avg}}$	$t_c$ (s)	$d_c$ (km)	$d_e$ (km)	$e_{\min}$ (%)
Denali	0.90	5.0	1000	0.96	-4.8	20	35	32
Kokoxili	0.83	5.0	500	0.95	-0.8	40	30	40

3 km/s scaling speed) of all previously accepted points. The final subset of points represents our most reliable estimates of the true locations of sources of radiated seismic energy. Table 1 indicates the back projection parameters used for each earthquake.

### 3.1. Kokoxili $M_w$ 7.8 Earthquake

[20] The 2001 rupture occurred along five fault segments. On the basis of surface mapping [Xu *et al.*, 2002; Lin *et al.*, 2002] and modeling of teleseismic body waveforms [Antolik *et al.*, 2004; Ozacar and Beck, 2004], the earthquake initiated at 35.95°N, 90.54°E on a ~30-km-long, east striking fault about 40 km south of the Kunlun fault and propagated northeast across an extensional graben to the western Kusai Hu segment of the Kunlun fault. From there it propagated eastward about 85 km to the Hong Shui River gorge and eastern Kusai Hu segment. Propagation continued for another 150 km and branched onto the Kunlun Pass fault, persisting for another 100 km and a total length of ~400 km. We use the term “main branch” to refer to the rupture along the segments of the Kunlun fault and the Kunlun Pass fault. The average and maximum slip reported by Xu *et al.* [2002] along the main branch is 2 and 7.6 m, respectively. The maximum slip reported by Lin *et al.* [2002] was 16 m. The total duration and moment of the rupture was about 120 s and between  $4.6 \times 10^{20}$  and  $5.3 \times 10^{20}$  N m [Antolik *et al.*, 2004; Ozacar and Beck, 2004].

[21] The first-motion pattern of this rupture can be explained by a pure strike-slip mechanism. However, the first 30 s of this rupture is best modeled as a combination of left-lateral slip propagating to the west, and normal slip propagating to the east-northeast, with an optimum single-mechanism of left-lateral, oblique slip [e.g., Ozacar and Beck, 2004]. The mechanisms found for the +30 s duration of this rupture were mostly left-lateral strike slip, consistent with the Harvard CMT [Antolik *et al.*, 2004; Ozacar and Beck, 2004], which is located close to Kusai Hu Lake.

[22] The Kokoxili earthquake was well recorded at teleseismic distances, mostly by the European and west Asian seismic stations but also by an IRIS PASSCAL 40-station array in Ethiopia. On the basis of the available data that passed the quality control criteria, we selected a subnetwork of stations to use in the back projection based on the polarities predicted by the first-motion and CMT focal mechanisms (Figures 2a and 2b). The cross-correlation analysis did not identify any polarity corrections that were required to align the data in the -3 to +6 s time window (Figure 2c). We attribute this to the length of the time window that we use in the cross-correlation analysis, which is long enough such that the waveforms are aligning on energy from the bilateral, oblique slip moment release, the mechanism of which does not predict polarity flips (Figure 2b). There were only a handful of other stations to the east of the hypocenter, but many of them did not pass

the quality control criteria. Of those that did pass, the polarities were not consistent for nearby stations, and were discarded.

[23] The 70 stations remaining for analysis are contained entirely within the same quadrant for the Ozacar and Beck [2004] 0–30 s moment mechanism, and the Harvard centroid moment mechanism. Consequently, any subevents in the rupture that are consistent with the Harvard CMT should not be attenuated in the back projection due to polarity changes. The seismic data show two distinct pulses of energy in the 0.2–0.9 Hz band that do not correlate with the timing of any standard seismic phases: between 10 to 20 s and 80 to 100 s (Figure 2d). The PP phase is predicted to come in at least 100 s following the direct P phase for almost all of the stations used in the analysis. The pulses of major moment release occur between 0 and 15 s, 65–75 s, and 85–100 s [Antolik *et al.*, 2004; Ozacar and Beck, 2004].

[24] Back projecting the teleseismic P waves illuminates the first 300–350 km of the rupture well. Figure 3 shows the RMS average of  $S_i(x, y, t)^2$  over 0–120 s. Reds indicate portions of the rupture that radiated energy that was phase coherent at the seismic stations. Tracking of the energetic points and visualization of time slices (Figure 4 and Movies S1–S4 in auxiliary material<sup>1</sup>) show an initial propagation from the hypocenter to the west and northeast, followed by a better constrained unilateral eastward propagation along the main branch.

[25] The easternmost part of the rupture is not well imaged. The rupture reaches the Harvard CMT location at about 70 s but then weakens in amplitude and bifurcates into two branches around 85 s: one propagates north and another continues propagating east until 115 s, the point at which coherence is completely lost, presumably due to rupture termination. The northward branch is likely an artifact due to a significant change in the 3-D velocity heterogeneity between one group of stations and the segment of the Kunlun fault east of the Harvard CMT. Evidence for this comes by analyzing a  $M_w$  5.6 aftershock located near the junction between the Kunlun fault and Kunlun Pass fault (Figures 3 and 4). We performed the cross correlation on the aftershock waveforms in the same frequency band as the main shock. The resulting time shifts were visually validated for all stations. Only four of the stations used in the main shock did not record the aftershock, and those stations were not used in the analysis. We back projected the aftershock waveforms using both the aftershock cross-correlation traveltimes corrections and the main shock traveltimes corrections (Figures S1–S4). Specifically, we obtained a 56% power reduction (34% amplitude reduction) when we use the main shock-determined corrections, suggesting an along-rupture change in the 3-D velocity heterogeneity between the rupture and the stations. The aftershock is still imaged in the correct location, but at a later time the energy diverges along two paths (Figure S2, 9–12 s). This is similar in amplitude and geometry to the bifurcation observed in Figure 4, 90–100 s (Movie S1 provides a better amplitude comparison) and suggests that the energy to the NW of the fault seen during 90–100 s

<sup>1</sup>Auxiliary materials are available in the HTML. doi:10.1029/2008JB005738.

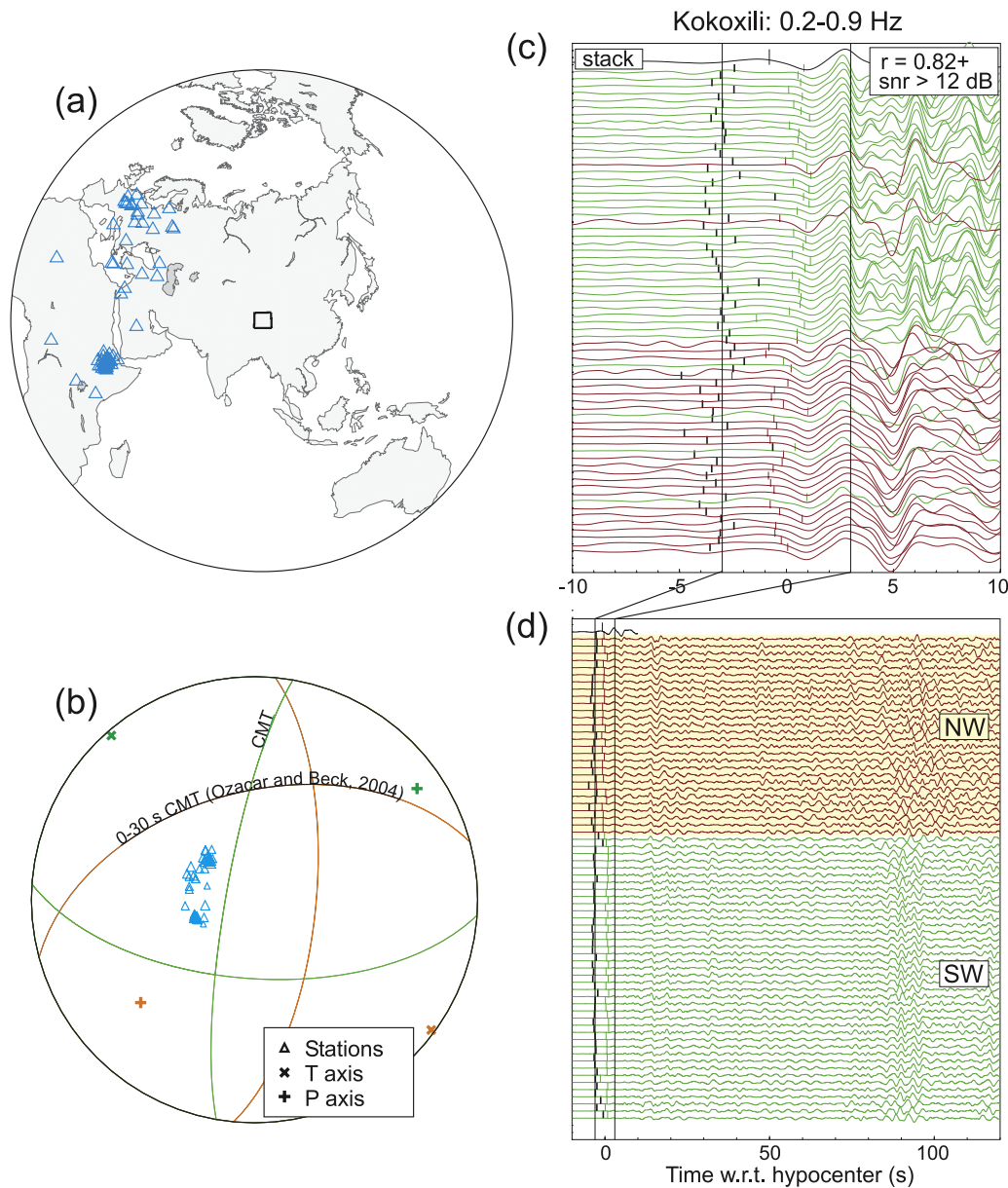


**Figure 2.** The 70 stations and P wave trains used in the back projection imaging of the Kokoxili rupture. (a) Map showing the back projection grid region (rectangle) and the seismic stations (triangles). The outer circle is the epicentral distance at  $90^\circ$ . (b) Lower hemisphere focal sphere showing the Harvard and 0–30 s Ozacar and Beck CMTs. Triangles indicate the station takeoff angles for the direct P phase. (c) Vertical component records of the P waves, aligned and sorted by correlation coefficient ( $r$ ; decreases from 0.99 from the bottom up) to the master stack (top trace). The time shifts required for alignment (relative to IASP91 predictions) are shown as thick ticks. Thin ticks indicate the pick determined by an STA/LTA autopicker. (d) Records sorted by azimuth to each station. Waveforms are normalized to have the same maximum amplitude in the cross-correlation time window. The source-receiver distance range is  $31^\circ$  to  $73^\circ$ .

maps back to a location on the fault during 80–90 s. Almost every other aftershock was not strong enough to be detected at most of the stations used in the imaging of the main shock, inhibiting efforts to use several aftershocks to carefully fine tune the teleseismic imaging. However, most of the rupture was imaged well enough to permit tracking of the rupture. Such aftershock corrections have a greater influence in higher frequency imaging. For example, *Ishii*

*et al.* [2007] performed such corrections to improve imaging the 2004 and 2005 Sumatra earthquakes with 1+ Hz waveforms recorded by the Japanese Hi-net array.

[26] The rupture speed can be measured by projecting  $S_i(x, y, t)^2$  onto a line parallel to the rupture. We use the single projection line shown in Figure 3, beginning 40 km west of the hypocenter and extending to the east. The lack of direct overlap with the fault segments is acceptable given

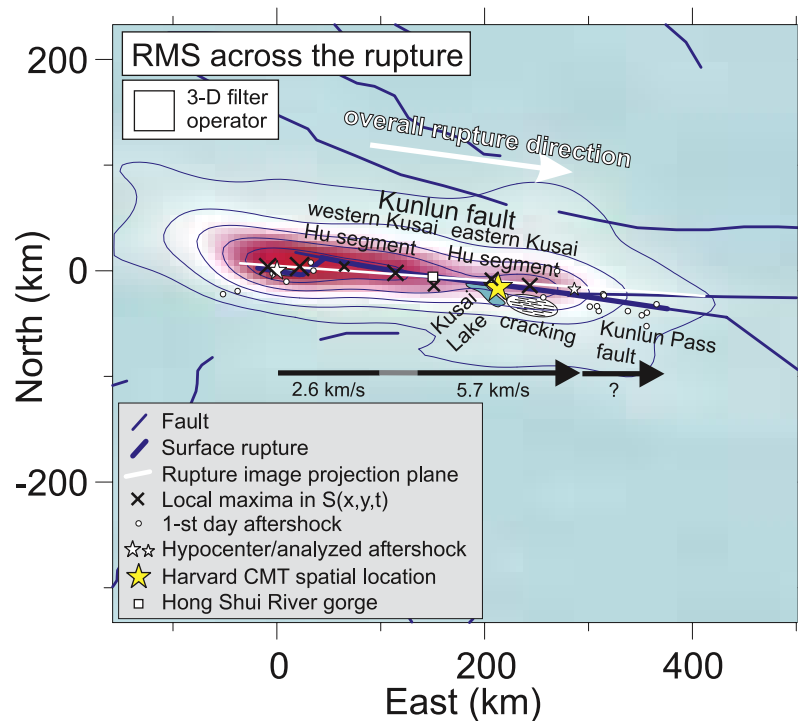


**Figure 3.** Back projection image of the Kokoxili rupture in map view. Color indicates the coherence of back projected energy from the first 130 s of the P wave train ( $\text{RMS}\{S_i(x, y, t)^2\}$ ). The northern and southern boundaries of the surface cracking to the south of the Kunlun fault [Bhat *et al.*, 2007] are not known and therefore are probably not drawn accurately.

our resolution of  $\sim 40$  km, which is based on our space-time smoothing operator. Figure 5 shows the RMS average within 50 km of the projection line. The slope in this plot is a direct measure of the rupture propagation speed. Energy traveling at the apparent teleseismic P wave speed of 14–22 km/s is indicative of arrivals that are not interfering constructively from one or more seismic stations located east of the rupture, close to the projection plane. Alternatively, energy with the same slope but mirrored about the  $y$  axis is from similar in-plane stations located west of the rupture. Although such energy would have also been partially attenuated by the 3-D integration filter, a minor amount remains in the hypocentral region and near 80–150 km.

[27] The back projection images and the positions of the energetic points have adequate resolution to unambiguously resolve two rupture speeds: 2.6 km/s between  $\sim 20$  and  $\sim 120$  km and 5.7 km/s between  $\sim 120$  and  $\sim 290$  km. The former is not as well constrained between 20 and 100 km because of the bilateral nature of the initial rupture, and the deviation of the strike of the graben fault from the projection line. The transition between the two speeds appears abrupt, but given our 40 km resolution, the transition seems to have occurred over a length no greater than 40 km.

[28] As discussed above, the trace amplitudes were normalized (AGC) to assist in the illumination of the entire rupture to obtain a more accurate rupture speed estimate. Therefore, the reds in Figure 5 indicate the relative distribution of energy that was phase coherent at the seismic stations. The time slices and animations show that the last 100 km of the rupture was not well imaged, which also

explains the lack of energy in Figure 5. However, there is a remarkable lack of energy from 25 to 40 s in Figure 5 that is not associated with mislocated energy in the time slices. This likely reflects a much smaller intensity or duration of energy radiated at the source during this time since the normal faulting mechanism that is mostly associated with this energy [Ozacar and Beck, 2004] would have yielded consistent polarities with those of the first 6 s (Figure 2b).

[29] Beginning at  $\sim 50$  s just west of the Hong Shui River gorge, the rupture coherence increases greatly and appears to have a consistent speed of  $\sim 5.7$  km/s. This 5.7 km/s segment correlates in time with the dominant components of the moment rate functions [Antolik *et al.*, 2004; Ozacar and Beck, 2004; Robinson *et al.*, 2006]. A local peak in two of the moment rate functions after 85 s correlates with the bifurcation discussed above.

### 3.2. Resolution and Uncertainty

[30] One of the advantages of using earthquake imaging to track the rupture in space and time, without regard for accurate amplitudes, is that it is relatively simple to determine when there is an imaging problem that affects resolution and uncertainty. Specifically, the manifestation of an imaging problem is energy that is mislocated or smeared over some distance, or energy that has separated into high-amplitude lobes that are not located along the rupture (i.e., the rupture is out of focus). The existence of such a problem is perhaps the easiest to determine for strike-slip faults because the fault plane is nearly vertical, and energy mislocation is therefore easy to spot. It is more challenging to evaluate the possibility of energy misplaced to another

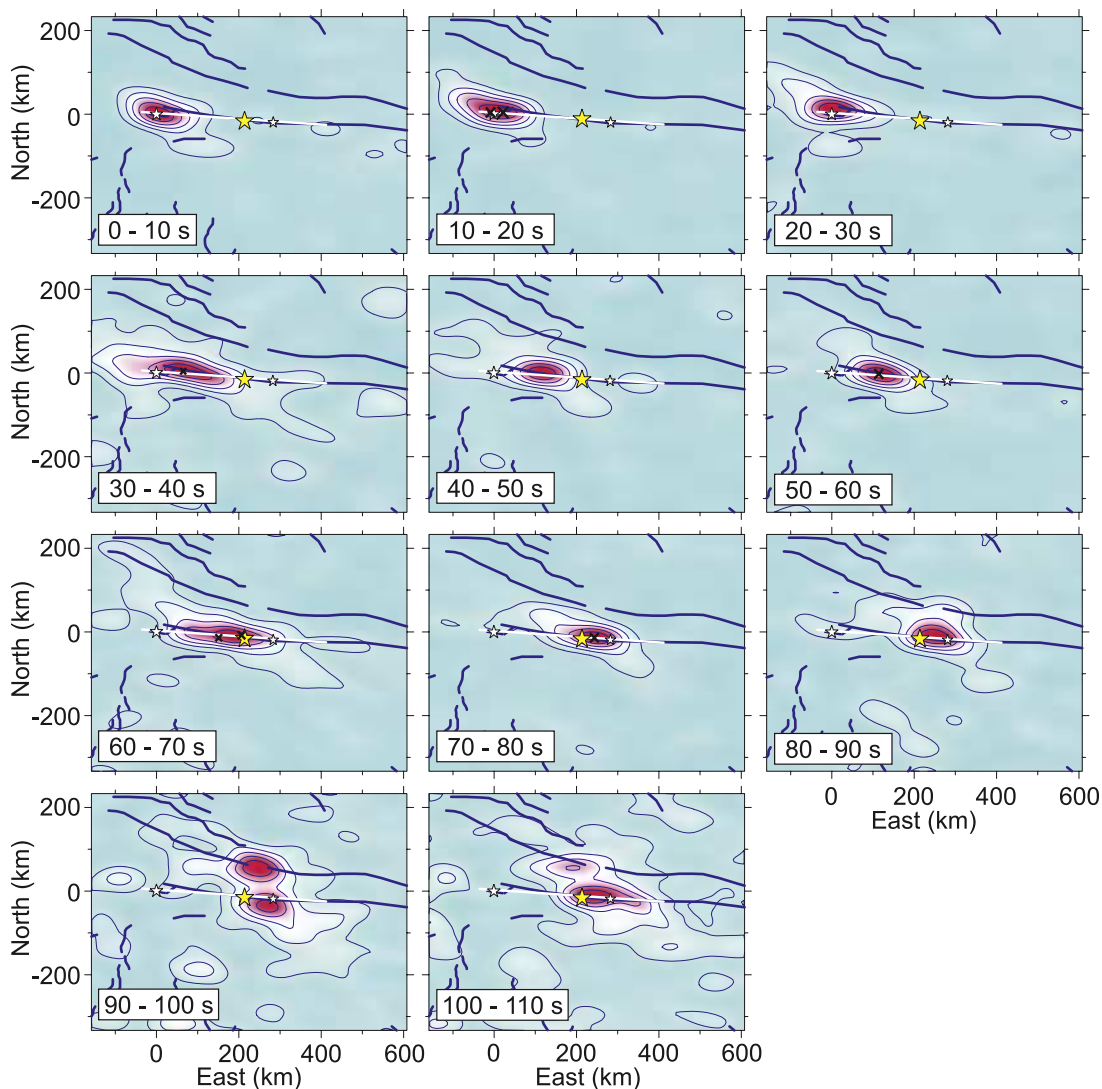


**Figure 4.** Back projection time slices showing the eastward Kokoxili rupture propagation. See Figure 3 for symbol explanation. Color indicates the coherence of back projected P wave energy ( $\text{RMS}\{S_i(x, y, t)^2\}$ ), which is normalized by the maximum in each time frame. No smoothing was applied between time frames.

location along the rupture. In all these cases, visualizing the data in different ways provides the most useful diagnostic. Figure 4 shows a probable resolution issue at about 90–100 s. Figure 5 shows a minor smearing toward the west with an apparent P wave speed. Fortunately these effects are minor and we are still able to accurately track the rupture front to 90 s.

[31] To further evaluate the theoretical resolution of our images and the stability of our results, we performed a number of synthetic tests using different parameters applied to the same station geometry that recorded the actual earthquakes. Our first test was to determine if we can resolve the difference between a subshear and supershear rupture. We created synthetic point source events (impulses) at the spatial locations of the energy peaks (the peaks in the smoothed  $S(x, y, t)$  function) obtained from our imaging analysis. For the synthetic supershear case, we also used the observed times of the energy peaks. For the subshear case, we assumed a rupture speed of 2.6 km/s for the entire

rupture and adjusted the times of the input points accordingly. The source amplitudes were assigned to the observed peak amplitudes. The point sources were then filtered with the same 0.2–0.9 Hz filter used for the real data. In other words, we created synthetic ruptures of two different rupture speeds assuming that each rupture gives rise to a series of 0.2–0.9 Hz filtered impulses that propagate outward in all directions to the same stations used in the imaging.

[32] Applying identical imaging parameters to those used previously, we find that the pulses of energy are correctly resolved, and slightly smeared along a negative rupture speed slope, reflecting the influence of the European stations to the northwest of the Kunlun fault (Figure 6). Note that the shape of the individual red clusters in Figure 6 is an estimate of the theoretical resolution kernel for a single point source. These energy peaks are not circular because of the nonuniform station coverage; they tend to be elongated in the direction of the bulk of the stations. Note that in this case the station geometry does not promote the smearing of

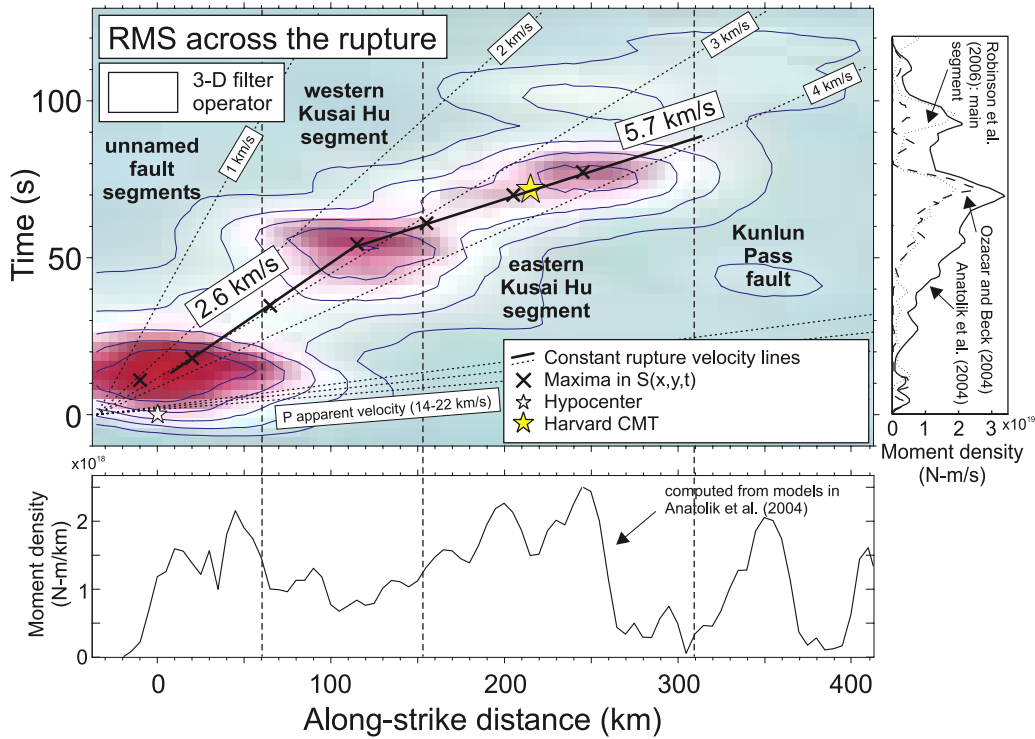


**Figure 5.** Back projection image of the radiated P wave energy along the Kokoxili rupture as a function of time. Shown is the RMS average of  $S_i(x, y, t)^2$  across the rupture projection line out to 50 km (see Figure 4). The spatial moment-density function was calculated from the preferred four-fault model of *Antolik et al. [2004]* and projected onto the same line as  $S_i(x, y, t)^2$ .

energy in the direction of propagation, which could result in an upward biased rupture speed estimate. The energetic points that are recovered are midway between the input energetic points. Additional tests showed that these energetic points are slightly mislocated due to smearing associated with the 3-D integration operator. Because this mislocation does not affect the rupture speed, we can clearly distinguish between the two cases, and recover the same input rupture speeds.

[33] We performed a number of other tests using different frequency bands, imaging parameters, and station networks. For example, we removed the restriction to include stations to the east of the hypocenter that were also within the consistent polarities region of the two focal spheres in Figure 2b, but that degraded the results. We also flipped the polarities of stations in a controlled fashion at specific times in the rupture, and found that we lose coherence at those points in the rupture.

[34] We also studied the effect of the back projection station weighting radius  $w_b$ . Values less than and greater than 500 km led to more smearing in the northeast direction (toward Europe). This is as expected, as too large or too small a radius will tend to weigh all stations equally. We determined by trial and error the optimum value of 500 km, which produces the least smearing of the resolution kernel, and which is a function of the source-station geometry, frequency content, and the degree of heterogeneity in station density.

[35] We also experimented with changing the scaling speed of 3 km/s used to smooth  $S(x, y, t)^2$  in space-time

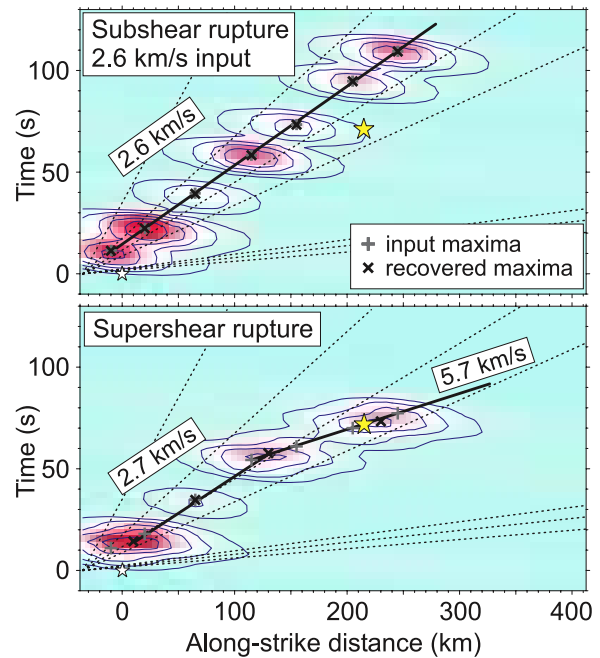


**Figure 6.** Synthetic tests for Kokoxili rupture imaging, showing results obtained for (top) a subshear rupture and (bottom) a supershear rupture, similar to that observed in Figure 5.

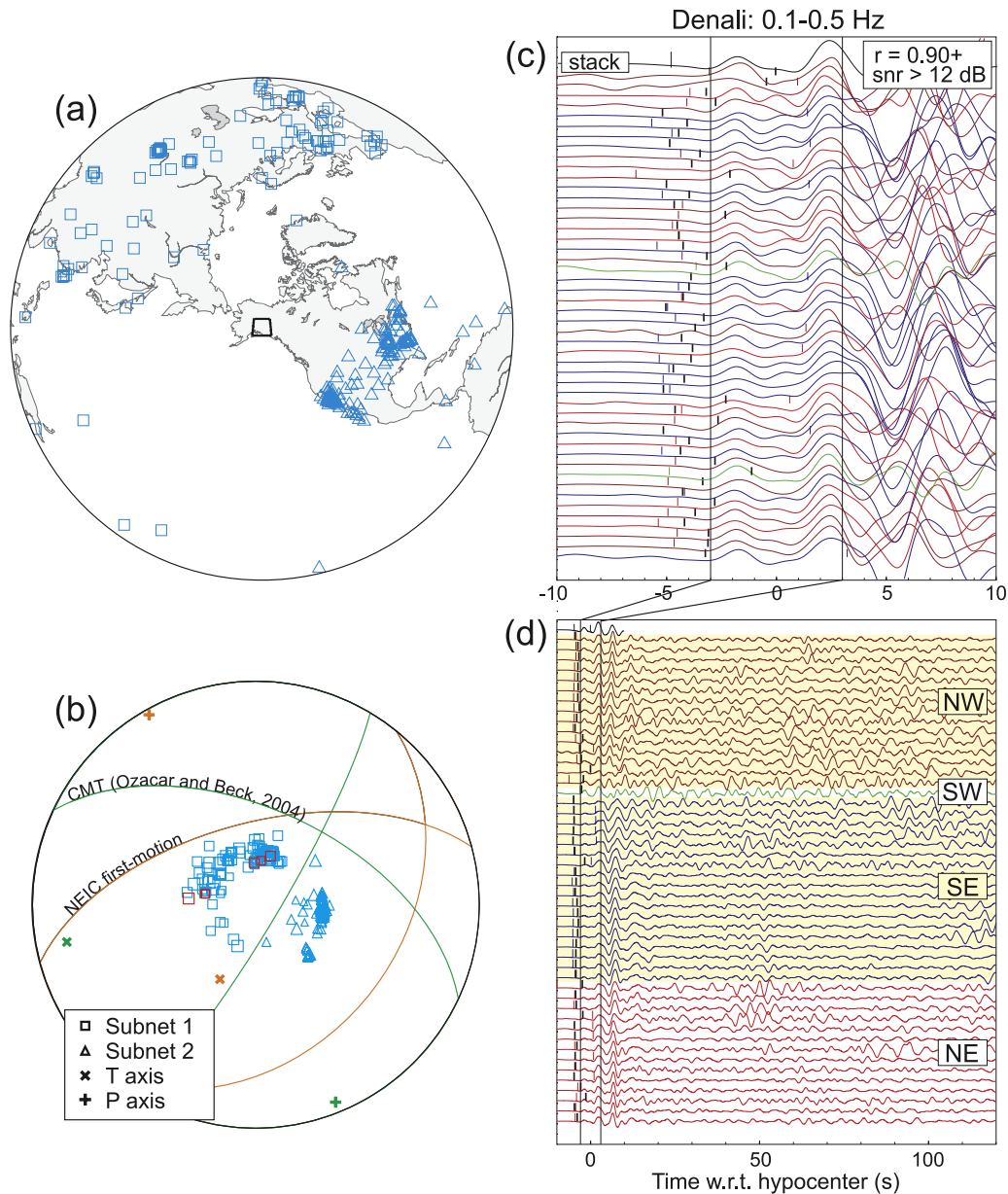


**Figure 7.** Stations and P wave trains used to image the Denali rupture. The stations were sorted into two subnetworks depending on their location with respect to the two focal mechanisms. (a) Map showing the back projection grid (black square) and the seismic stations (squares for subnet 1 and triangles for subnet 2). A black (or red online) symbol indicates a station for which a polarity correction was applied. The outer circle is at an epicentral distance of  $90^\circ$ . (b) Lower hemisphere focal sphere, showing the NEIC first-motion solution and the CMT solution of *Ozacar and Beck* [2004]. Station takeoff angles are shown for each subnetwork. Station color indicates the optimum polarity determined by cross-correlation analysis. (c) Vertical component records of the P waves, aligned and sorted by correlation coefficient to the master stack (top trace). The time shifts required for alignment (relative to IASP91 predictions) are shown as thick ticks. Thin ticks indicate the pick determined by an STA/LTA autopicker. (d) Records sorted by azimuth to each station. Waveforms are normalized to have the same maximum amplitude. The source-receiver distance range is  $30^\circ$  to  $98^\circ$ .

and obtained slightly different results for different speeds. Removal of the filter yielded images that were higher in frequency, but did not greatly affect our overall results. This test along with other tests involving the station weighting radius,  $d_c$ , and  $d_e$  indicate that we cannot rule out supershear

speeds anywhere between 4.7 and 6.5 km/s, although 5.7 km/s is the most reliable estimate.

[36] Last, we also tried to back project traces from the IRIS PASSCAL Ethiopian array, which had an aperture of about 500 km. We used higher frequency ranges of 0.5–4.0 Hz and 0.8–4.0 Hz. The trace alignment obtained was

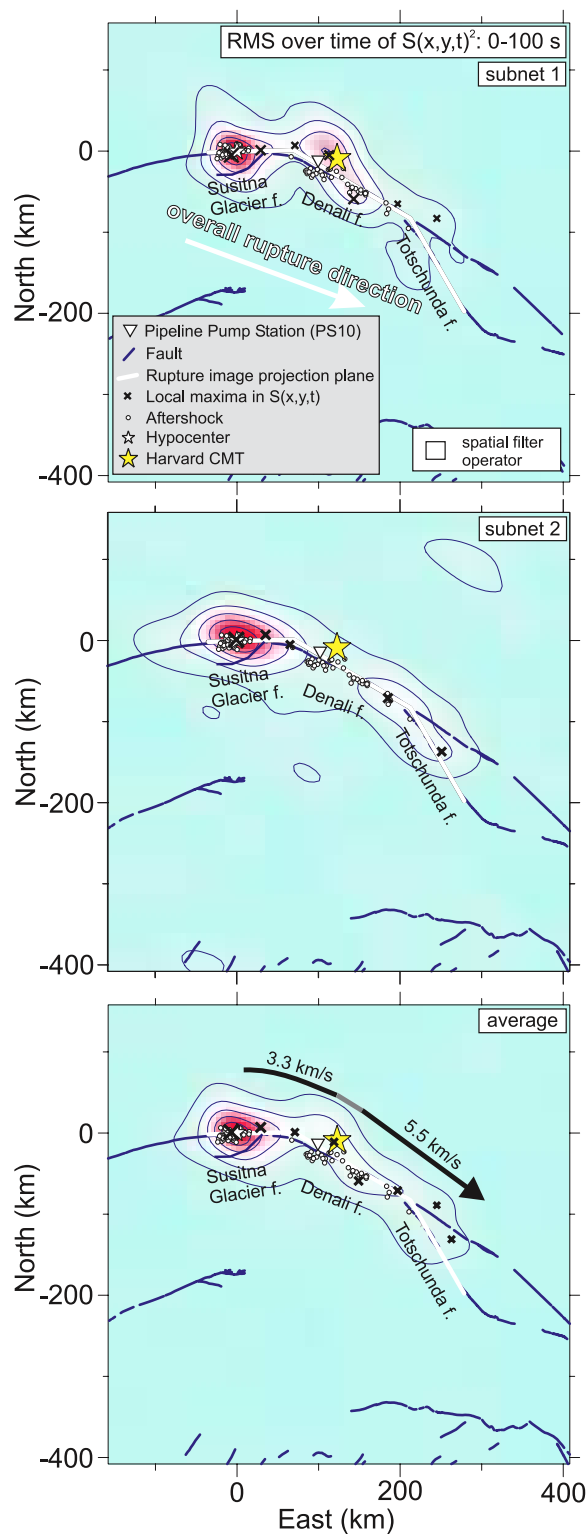


**Figure 8.** Back projection image of the Denali rupture in map view. Color indicates the coherence of back projected P wave energy for subnets 1 and 2 and their average ( $\text{RMS}\{S_i(x, y, t)^2\}$ ).

excellent, but the source-station geometry was too poor or changes in the along-rupture 3-D velocity heterogeneity between the rupture and the array were too great to unambiguously resolve any features of the rupture.

### 3.3. Denali $M_w$ 7.9 Earthquake

[37] The 2002 Denali rupture occurred along three fault segments [Eberhart-Phillips *et al.*, 2003]. From surface offset mapping, the Denali rupture initiated at  $63.52^\circ\text{N}$ ,  $147.44^\circ\text{W}$  on the previously unrecognized Susitna Glacier reverse fault and propagated west for about 48 km [Haeussler *et al.*, 2004]. At some point during this time, rupture initiated on the McKinley strand of the Denali fault system and proceeded eastward 70 km to the main segment of the Denali fault. This is also the location of the Trans-Alaska Pipeline, where a strong motion station, PS10, recorded the ground motion [Ellsworth *et al.*, 2004]. From this point, the rupture continued to the east another 156 km, stepped across a  $\sim 20$ -km-long transfer zone, and propagated southeast along the Totschunda fault for another 66 km, yielding a total surface rupture length of 341 km [Eberhart-Phillips *et al.*, 2003; Haeussler *et al.*, 2004].

[38] Vertical slip on the Susitna Glacier reverse fault averaged about 4 m at the surface [Crone *et al.*, 2004], while the average and maximum horizontal slips on the Denali fault were 5 and 9 m, respectively. Horizontal slip on the Totschunda fault averaged about 2 m [Eberhart-Phillips *et al.*, 2003; Haeussler *et al.*, 2004].

[39] In contrast to the Kokoxili earthquake, the Denali fault earthquake was well recorded at local, regional, and teleseismic distances. There are a total of 242 station traces that pass the quality control measures previously discussed. However, the final seismic recordings that are back projected are sorted into two subnetworks. The rupture initiation is well represented by the first-motion mechanism [Ozacar and Beck, 2004], and we find that our cross-correlation analysis on the 0.1–0.5 Hz data only flags a few of these stations for polarity flips (Figures 7a and 7b). However, the rest of the rupture is not similar to the first 35 s. We therefore adopt the moment tensor solution of Ozacar and Beck [2004] for the 35+ s of the rupture, which is derived by “pulse stripping” the first 35 s from the data, then modeling the rest for a single-event model. We then sort stations into two subnetworks depending on their location with respect to the two mechanisms. In each subnetwork, there are no changes in predicted polarities between stations for each focal mechanism (Figure 2b). However, if we simply back projected the entire network of stations, there would be significant attenuation along most of the rupture due to destructive interference. Subnet 1 and 2 contain 102 and 140 stations, respectively.

[40] As has been documented already, there is remarkable directivity in the 0.1–0.5 Hz band [Eberhart-Phillips *et al.*, 2003; Frankel, 2004] (Figure 7d). The first 10 s of the rupture contains the greatest amount of P wave energy. This may in part be due to the mechanisms; the reverse-faulting mechanism predicts high amplitudes in the initial part of the rupture, but the stations are closer to the P nodal planes for the Ozacar and Beck 35+ s subevent mechanism. The only visibly coherent energy in the time series after 35 s is for stations to the southeast of the rupture around 50 s.

[41] The optimum back projection of these data comes from processing subnet 1 and 2 separately and averaging the two  $S_i(x, y, t)^2$ . The map view RMS averages for 0–100 s are shown in Figure 8. Both subnetworks illuminate the entire fault rupture, and the energetic points line up approximately along the ruptured fault as expected. However,

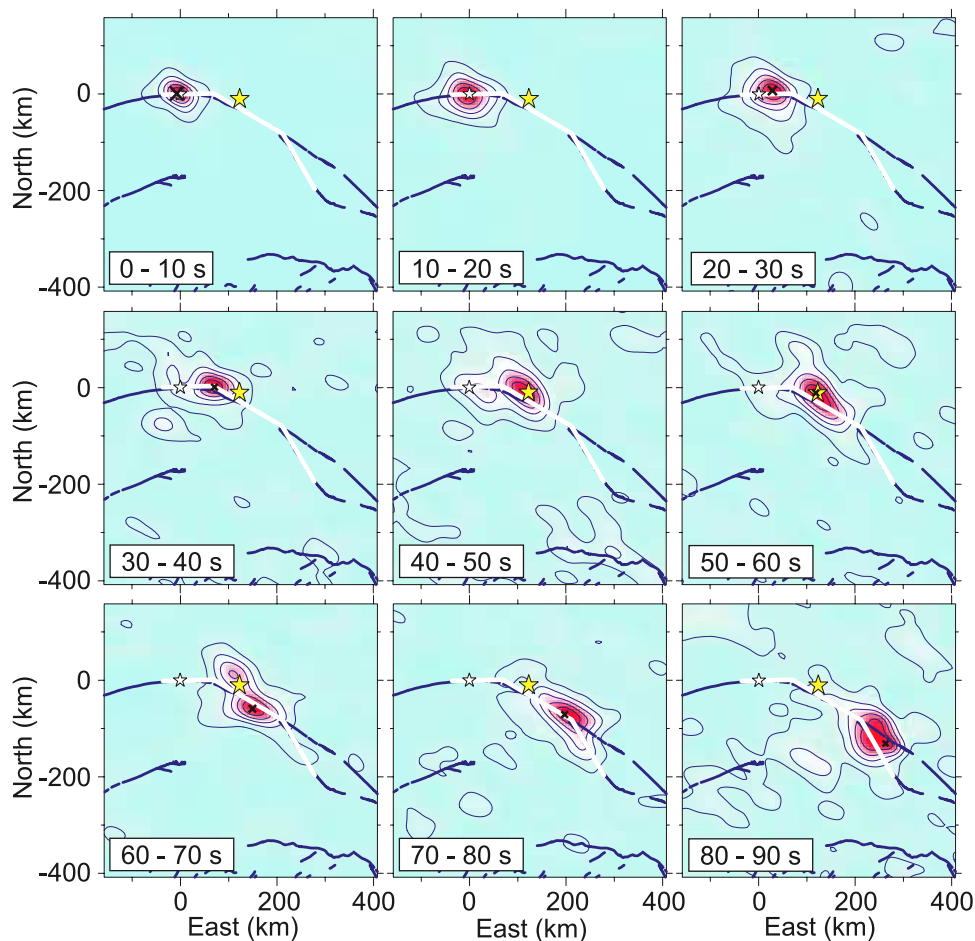


**Figure 9.** Back projection time slices ( $\text{RMS}\{S_i(x, y, t)^2\}$ ) showing the Denali rupture propagation. See Figure 8 for symbols. The time slices resolve an initial 0–20 s of westward rupture propagation before the subsequent eastward propagation. No smoothing was applied between time frames.

subnet 1 images the hypocenter and the first 200 km of the Denali rupture better than subnet 2, whereas subnet 2 images the far end of the rupture better. The average (also shown in Figure 9) yields a more continuous distribution of energy along the rupture is our preferred result with which to measure rupture velocity. However, both subnetworks resolve more coherent P wave energy at the hypocenter than anywhere else along the rupture.

[42] The time slices and animations show good coherence out to 90 s, indicating that the rupture is fairly well imaged out to its termination on the Totschunda fault (Figure 9). The rupture starts on the Sustina Glacier fault and continues toward the west for the first 20 s. It then propagates east along the McKinley strand of the Denali fault system to the junction with the Denali fault at PS10 at about 40 s, which is consistent with the first arrival and fault-normal arrival of the rupture front at PS10 (37 and 40 s [Ellsworth *et al.*, 2004]). An increase in coherence begins at about 50 s as the rupture propagates along the Denali fault to the Totschunda fault junction. From the junction until the end of the rupture at 90 s, the resolution is not adequate to differentiate between rupture on the Denali or Totschunda faults. As was done by Ishii *et al.* [2007], one could use aftershocks to correct for the apparently minor effect of along-rupture changes in 3-D source-station velocity heterogeneity, but almost all

aftershocks were too small to be well recorded at the stations used in the teleseismic imaging of the main shock.

[43] The images of the rupture across the fault as a function of time also show the resolution capabilities of each subnetwork (Figure 10). Subnet 1 resolves the initial rupture to the west along the Sustina Glacier fault at a horizontal speed of  $\sim 2.5$  km/s. About 20 s later, rupture begins to propagate to the east along the Denali fault at an estimated rate of 2.9 km/s to the Harvard CMT location (km 130), where the rupture accelerates to 4.5 km/s. Subnet 2 (mostly North American stations) is associated with more smearing than subnet 1 because of the more limited distribution of stations. The smearing is in the direction of propagation at the apparent P wave speeds. Regardless of this smearing, energetic points and centers of significant energy suggest 2.7 km/s for the first 60 km of eastward propagation, and 4.9 km/s for propagation along the Totschunda fault. However, we consider the images using the average  $S_i(x, y, t)^2$  to be the most reliable. These results suggest 3.3 km/s out to km 130 and 5.5 km/s out to a distance of 330 km.

### 3.4. Resolution and Uncertainty

[44] In a similar fashion to the Kokoxili rupture, we performed synthetic and other tests to determine the robust-

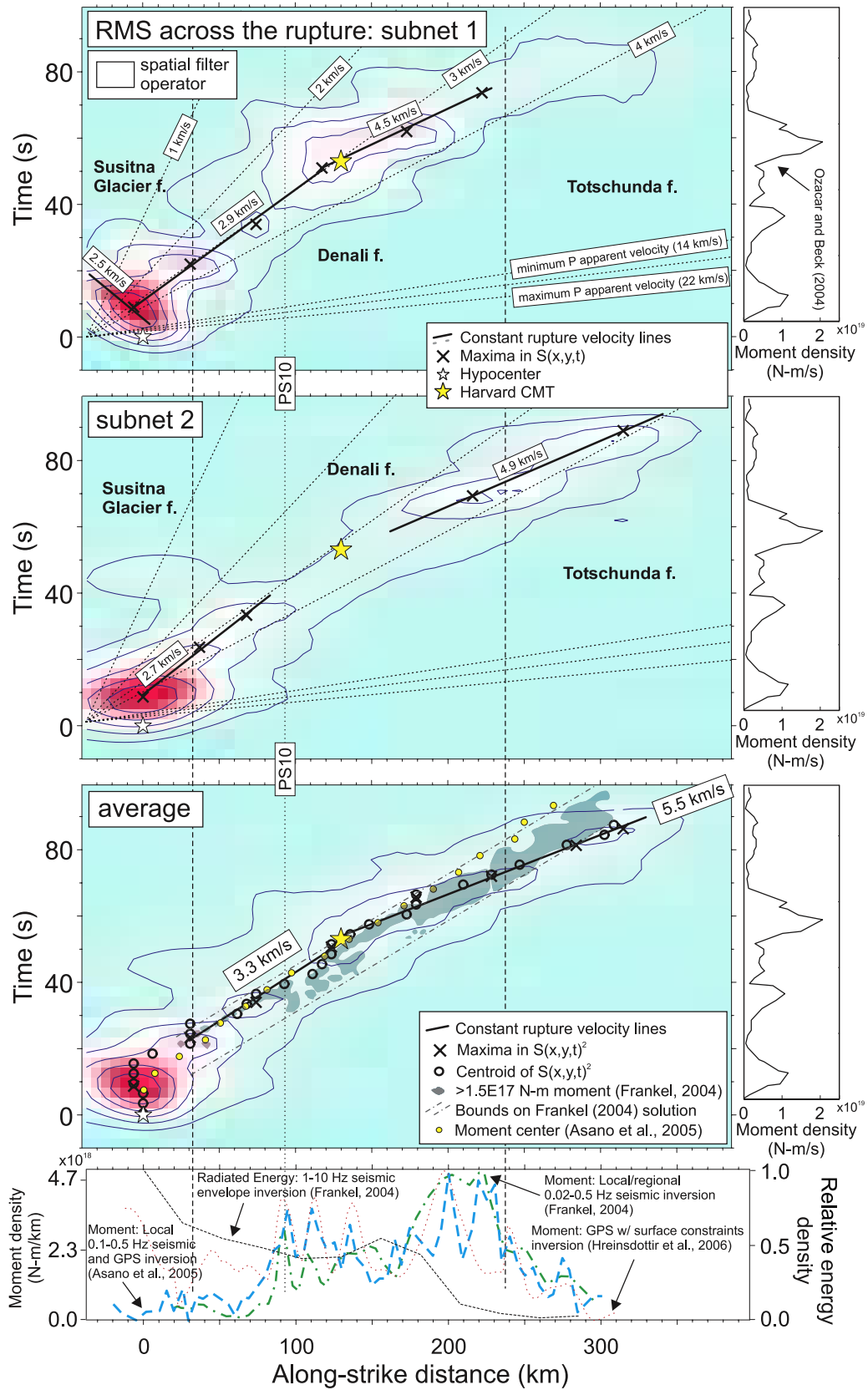


**Figure 10.** Back projection image of the radiated P wave energy along the Denali rupture as a function of time. Shown is the RMS average of  $S_i(x, y, t)^2$  across the rupture projection line out to 50 km (see Figure 9). The moment density results were obtained by *Frankel [2004]*, *Asano et al. [2005]*, and *Hreinsdóttir et al. [2006]* (calculated from their model and projected onto the same lines).

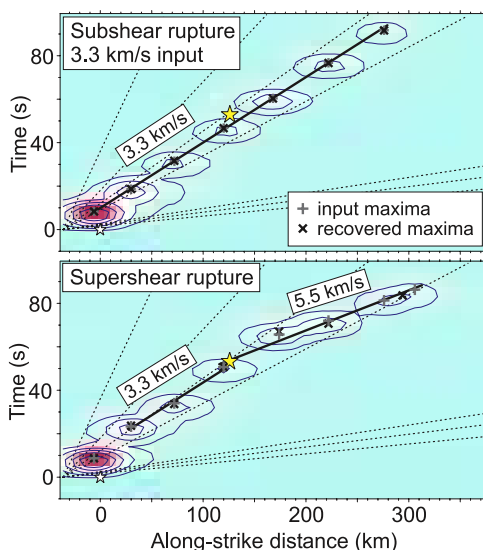


**Figure 11.** Synthetic tests for Denali rupture suggesting that the specific supershear rupture resolved in Figure 10 is clearly distinguishable from a subshear rupture.

ness of our rupture speed estimates (Figure 11). For the subshear case, we chose a rupture speed of 3.3 km/s for the entire rupture, consistent with the first part of the rupture in our preferred image (Figure 10). For the supershear case, we again used the energetic points from Figure 11 as the input subevents. The synthetic tests show that we are able to clearly discriminate between the subshear and supershear cases, and that we recover both the amplitudes and positions of the input energetic points better than for the Kokoxili rupture. This improved resolution is due mostly to the improved station coverage, which also allowed us to use a smaller 3-D integration operator (20 km versus 40 km for the Kokoxili rupture).

[45] Our imaging suggests that the strike-slip motion on the Denali fault system began about 20 s following rupture initiation. *Ozacar and Beck* [2004] inverted for moment distribution on both the reverse-faulting subevent and the strike-slip component of the main rupture. Instead of using two subnetworks independently and adding their respective  $S_i(x, y, t)^2$ , we tried to use the entire network by flipping the polarity of the traces from subnet 2 after 30 s such that they should be in phase along the main part of the rupture during the back projection. The images were significantly degraded. Specifically, the rupture was discontinuous and lower in power than that in Figure 10. We also back projected all the waveforms without flipping the polarity of subnet 2 and energy was imaged better in some locations along the rupture, but the overall rupture image was worse. The result of our tests indicated that for the supershear segment that we image, 5.5 km/s is our most reliable estimate, although as with the Kokoxili earthquake, we cannot exclude speeds between roughly 4.5–6.5 km/s.

## 4 Discussion

### 4.1. Poorly Constrained Parts of the Ruptures

[46] The first three quarters of the Kokoxili earthquake are fairly well imaged with the network of stations to the

west of the rupture. However,  $S_i(x, y, t)^2$  loses some coherence east of Kusai Lake where the energy splits into two branches, one that moves  $\sim 100$  km northward, and the other continuing east along the Kunlun Pass fault (Figures 3 and 4 and the auxiliary material). The probable explanation for this is a significant change in the 3-D velocity heterogeneity along source-receiver raypaths for the Eurasian or African stations. For this model, simple geometrical relationships indicate that a 5 s time shift for either group of stations is needed to create this bifurcation. This is consistent with a comparison of the main shock traveltimes corrections with those obtained by cross-correlation analysis of waveforms from a  $M_w$  5.6 aftershock near the Kunlun Pass junction. The analysis shows that about a quarter of the stations (all from the Ethiopia-Kenya region) have a difference of 3 to 7 s in their respective optimum travel time correction to account for 3-D velocity heterogeneity.

[47] Another possibility is that the intensity of radiated energy may have quickly decayed along the rupture at 90–100 s such that waveform coherence at the stations is generally lost and energy that was correctly located earlier in time still dominates. If that is the case, the energy in the 100–110 s time frame is likely correctly located, which would indicate that we image almost the entire  $\sim 400$ -km-long rupture (Figures 4 and 5). *Dunham et al.* [2003] performed a series of numerical experiments and found that stronger along-fault barriers can focus the rupture front, leading to an order of magnitude increase in slip speed and radiated seismic energy. This may be a physical explanation for the high burst of energy observed just before the dramatic loss of coherence. Another possible physical mechanism for the reduction in seismic radiation intensity may be the transition onto the Kunlun Pass fault, which has a different geometry than the long and straight Kunlun fault [*Robinson et al.*, 2006; *Das*, 2007] and may have had a different strength or preslip stress.

[48] The Denali rupture was fairly well imaged with two subnetworks instead of using the entire network (with or without polarity flips), with or without polarity flips to adjust for the two different primary source mechanisms. Although there is a marked decrease  $S_i(x, y, t)^2$  along the length of the rupture, the power levels remain significantly above the noise level. These two observations mean that either the waveform coherence of the rupture was better in some directions than in others, or the 3-D velocity heterogeneity time shift corrections obtained by the cross-correlation analysis for the hypocenter-station raypaths do not adequately correct for 3-D velocity heterogeneity along the entire rupture. We suggest that the primary mechanism is a lack of global waveform coherence. First, there is already ample evidence for strong directivity associated with this rupture [e.g., *Eberhart-Phillips et al.*, 2003] (Figure 7d). Second, the strike-slip part of the Denali rupture was not along a straight fault, but along a series of faults that gave rise to a 60 degree rotation in strike, which is likely to produce changing directivity and focal mechanism effects along the rupture. For example, a coherent waveform packet is observed for many of the southeast stations at about 50 s that is not coherent elsewhere (Figure 7d). Third, time animations do not show evidence of defocusing, as there is generally a single center of high power along the rupture until about 90 s on the Totschunda fault. Finally, when

**Table 2.** Review of Rupture Speeds Estimated for the Kokoxili and Denali Ruptures<sup>a</sup>

Rupture	Location	Rupture Speed (km/s)	Method	Reference
Denali	120–160 km	3.5	Multiple window inversion of regional seismic data	<i>Frankel [2004]</i>
	<b>160–250 km</b>	<b>5.0</b>		
Denali	65–230 km	3.4	Multiple window inversion of regional seismic/GPS data	<i>Asano et al. [2005]</i>
Denali	70–80 km	3.5–4.1	Same	<i>Asano et al. [2005]</i>
	120–145 km			
	230–240 km			
Denali	average	3.2	Pulse stripping inversion of teleseismic P data	<i>Ozacar and Beck [2004]</i>
Denali	average	3.3	Multiple window inversion of regional seismic/GPS data	<i>Dreger et al. [2004]</i>
Denali	<b>60–90+ km</b>	<b>1.5<math>V_s</math> (~5.1)</b>	Forward modeling PS10 seismic data	<i>Dunham and Archuleta [2004]</i>
Denali	maximum	3.3	Inversion of apparent source time functions	<i>Liao and Huang [2008]</i>
	minimum	2.6		
	average	3.0		
Kokoxili	0–6 s	1.0–3.0	Point source inversion using teleseismic P/SH	<i>Antolik et al. [2004]</i>
	0–30 s	0–2		
	15–120 s	3.1–4.3		
Kokoxili	15–120 s	3.5	Finite fault inversion using teleseismic P	<i>Antolik et al. [2004]</i>
Kokoxili	average	3.4	Pulse stripping inversion using teleseismic P	<i>Ozacar and Beck [2004]</i>
Kokoxili	average	3.4	Pulse stripping inversion using teleseismic P/SH	<i>Lin et al. [2003]</i>
Kokoxili	0–100 km	~2.4	Surface wave analysis	<i>Bouchon and Vallée [2003]</i>
	<b>100–400 km</b>	<b>~5</b>		
Kokoxili	0–120 km	3.3	Inversion using teleseismic SH	<i>Robinson et al. [2006]</i>
	<b>120–270 km</b>	<b>6.7</b>		
Kokoxili	0–150 km	~3	Back projection of P waves using Nepal stations	<i>Vallée et al. [2008]</i>
	<b>150–300 km</b>	<b>~6</b>		

<sup>a</sup>Distance and time are with respect to the hypocentral parameters. The multiple time window inversions were some variation of the *Hartzell and Heaton [1983]* technique. The pulse-stripping inversion was based on the technique by *Kikuchi and Kanamori [1982]*. Unambiguous supershear speeds are indicated in bold and are discussed in the text.

subnets 1 and 2 are back projected independently, which generally reduces the possibility and impact of 3-D velocity heterogeneity changes along the entire rupture, only distinctly different parts of the rupture are illuminated, suggesting that only these rupture segments radiated coherent energy to their respective subnetworks.

#### 4.2. Comparison to Previous Work

[49] The resolution tests and other experiments that we performed suggest that we can measure rupture speeds on the supershear segments of the Kokoxili and Denali faults accurately enough to exclude the possibility of subshear speeds. The range of speeds for both cases is roughly 4.5 to 6.5 km/s, with the most reliable values being 5.7 and 5.5 km/s for the Kokoxili and Denali ruptures, respectively.

[50] There have been a number of rupture speeds reported for the Kokoxili rupture (Table 2). Most of these speeds range from 2.0 to 4.0 km/s and were derived by inverse modeling the seismic moment distribution using long- to intermediate-period seismic data. Reports of supershear speeds with uncertainties that probably exclude subshear speeds are from *Bouchon and Vallée [2003]*, *Robinson et al. [2006]*, and *Vallée et al. [2008]*. *Bouchon and Vallée* analyzed surface waves recorded by regional broadband stations. For four 100-km segments of the fault, they found rupture speeds of 2.4, 5.0, 4.8, and 5.0 km/s. These values are not precisely constrained, especially the last segment of the rupture. *Robinson et al.* inverted teleseismic SH waveforms to track the rupture front. They found a rupture speed of 3.3 km/s during the first 120 km, and a higher speed of 6.7 km/s between 120 and 270 km where we find a speed of 5.7 km/s supershear speed (Figure 5). A rupture speed closer to 5.7 km/s is also consistent with the results of *Robinson et al.* if the interpreted segment is extended to

350 km. After 350 km, the rupture front they find was poorly resolved and not reliably trackable, similar to what we observe at about 300 km (Figure 4). *Vallée et al. [2008]* also find evidence for supershear rupture speeds close to the P wave speed by analyzing seismic data from the regional Nepal broadband array.

[51] There have also been a number of rupture speeds in the 3.0 to 4.0 km/s range reported for the Denali rupture (Table 2). A supershear speed far from the subshear speed regime is reported by *Frankel [2004]*. He analyzed local and regional 0.02–0.5 Hz broadband waveforms, and high-frequency envelopes recorded by strong motion stations. He inverted the broadband waveforms for the spatiotemporal moment distribution. Although he constrained his moment solution to occur along the fault within 14 s of two 3.5 km/s rupture speed lines, some key features in his solution match our imaging results. Leading up to PS10, the centroids of 3 s back projection time slices show that the energy in the first part of the rupture tracks *Frankel's* results. Starting at km 130, *Frankel* fits a line with a 5 km/s slope along the leading edge of his moment distribution and extending to km 250 where it intersects the model solution lower boundary. Our images agree with this, and provide a means of extending *Frankel's* interpretation farther east. *Asano et al. [2005]* inverted local 0.1–0.5 Hz seismic and GPS-measured static displacements using a multiple time window, linear, kinematic waveform inversion. The positions of their moment centers do not agree with our imaging results, or those of *Frankel [2004]* (Figure 10).

[52] Our results suggest supershear speeds along at least 200 km of the Kokoxili and Denali ruptures. There have been other reports of supershear or near-supershear rupture speeds, but they are for smaller earthquakes. The 1979 Imperial Valley earthquake in California was reported to

have an average rupture speed of 2.5–3 km/s [Hartzell and Heaton, 1983], with a short patch of supershear rupture (4–5 km/s [Olsen and Apsel, 1982; Archuleta, 1984; Spudich and Cranswick, 1984]). The 1992 Landers earthquake appeared to have an average rupture speed of 2.7–3.0 km/s on the basis of strong motion seismic data and geodetic data from GPS and radar interferometry [Hernandez et al., 1999] and 5 km/s on the basis of a finite difference simulation [Olsen et al., 1997]. For the 1999 Izmit earthquake, Sekiguchi and Iwata [2002] modeled strong motion data recorded by ten stations and inferred a rupture speed of 5.8 km/s along the middle third of the rupture. S-P times from two strong motion stations were interpreted by Bouchon et al. [2000, 2001] in terms of an average eastward supershear rupture of 4.7–4.9 km/s and 4.3 km/s for the subsequent Duzce earthquake.

[53] If seismic moment and seismic energy release are proportional during an earthquake, one should expect agreement between rupture speeds estimated by back projection imaging and seismic moment inversions. We generally do not find this agreement (Table 2) because the majority of the finite slip models do not exhibit supershear rupture speeds. On the other hand, the high rupture speeds obtained by the moment inversions of Frankel [2004] (5.0 km/s) for the Denali rupture and Sekiguchi and Iwata [2002] (5.8 km/s) for the Izmit rupture suggest that relaxing certain solution constraints, or using constraints directly from back projection imaging, may be necessary to yield consistent results between the two approaches for very long strike-slip earthquakes.

[54] If seismic moment and seismic energy release are correlated, seismic energy and global phase coherence are correlated, and no imaging problems exist, one would also expect the moment distributions in time and space from other techniques to correlate with the distribution of  $S(x, y, t)^2$  along the fault. The spatial moment density estimated by Hreinsdóttir et al. [2006] (Figure 10) is similar to that by Frankel [2004] and Asano et al. [2005] for the Denali rupture. Although the spatial moment distribution does not correlate with most features in  $S(x, y, t)$ , the temporal moment rate function [Ozacar and Beck, 2004] does correlate to some degree, especially with the results using subnet 1. The same is true for the Kokoxili rupture (Figure 5). This may also suggest that the rupture speeds in the moment inversions were controlled too tightly.

[55] Inverting 1–10 Hz waveform envelopes for the source factor relative to the M 6.7 Nenana Mountain earthquake (Denali preshock) assuming a 3.0 km/s rupture speed yields a curve that matches the 0.2–0.9 Hz back projection power distribution for subnet 1 (Figure 10). The distribution for subnet 2 may not match because the stations used by Frankel span most of the azimuthal range, except to the east and southeast where subnet 2 is located. This also supports the hypothesis that the two subnetworks image different parts of the rupture because of variations in regional phase coherence. However, these comparisons are also limited in general by the fact that the frequency distributions are different and the rupture speed that we image appears to change along the fault. Frankel also tried a single 3.5 km/s rupture speed, but that produced an envelope at PS10 that did not fit the data as well.

#### 4.3. Implications for Material Properties

[56] The imaged transitions from subshear to supershear rupture speeds that approach the local P wave speed are consistent with that observed in laboratory experiments on the dynamics of mode II shear crack growth. These transitions relate to the mechanical strength of the fault. Rosakis et al. [1999] made laboratory measurements of crack growth along a preexisting plane separating two bonded plates of Homalite, a linearly elastic polyester resin that is representative of a class of materials that experience brittle fracture and stress-induced birefringence. Their primary observations confirmed certain predictions of the Burridge-Andrews propagation model (BAM), including the stability range of supershear rupture propagation between  $\sqrt{2} V_s$  and  $V_p$ , where  $V_s$  and  $V_p$  are the S and P wave speeds [Andrews, 1976; Burridge et al., 1979]. Rupture propagation in the Homalite experiments began close to the Rayleigh wave speed ( $V_R$ ), accelerated to a supershear speed close to  $V_p$ , and then decelerated to  $\sqrt{2} V_s$  for the remainder of the rupture.

[57] There were a few observed inconsistencies with the BAM model, including the finite structure of the Mach waves, the formation of secondary tensile microfractures trailing the shear crack tip, and issues concerning the stability and speed of the crack tip. Rosakis [2002] and Samudrala et al. [2002] explained these observations with a semi-infinite crack model where rupture propagation depends on (1) a slip rate weakening cohesive zone of a characteristic distance ahead of the rupture tip and (2) a constant crack tip sliding displacement criterion. The slip rate weakening parameter,  $\beta$ , is defined as a linear rate of change of the steady state coefficient of sliding friction with slip rate [Ruina, 1983; Rice and Ruina, 1983; Kilgore et al., 1993; Kato and Hirasawa, 1996]. The dependence of friction on the local “state” was ignored. The model states that a point along the locked fault undergoes an instantaneous jump in slip rate (from zero) as the rupture front passes. The dynamic strength of the fault reduces by an amount proportional to the slip rate. The static fault strength returns as the slip rate then decays behind the rupture front. These stability results have also been found by Burridge et al. [1979] and Freund [1979] using a slip-weakening law.

[58] On the basis of past theoretical and numerical work and their recent lab results, Rosakis [2002] and Samudrala et al. [2002] suggest relationships between the critical far-field shear stress required to sustain dynamic crack growth, the velocity weakening parameter, and the shear strength of the interface. These relationships can be interpreted as predictors of regions of stable rupture speeds. We can therefore relate our rupture speed observations to these stability regions and make inferences as to the mechanical properties of the ruptured faults. Zhao and Zeng [1993] used P and S wave arrivals from local Tibetan Plateau earthquakes to find an average P and S wave upper crustal speed of 5.6 and 3.3 km/s. Jin and Herrin [1980] inverted surface waves along the western Denali fault from North Pacific earthquakes to derive an average P and S wave upper crustal speed of about 5.8 and 3.4 km/s. We have plotted some of the Rosakis results in Figure 12, using crustal seismic speed values of  $V_p = 5.8$  km/s and  $V_s = 3.4$  km/s. The  $y$  axis is the critical far-field shear stress (required to satisfy the critical crack tip sliding displacement criterion) acting on the interface some distance  $D$  ahead of the cohesive zone

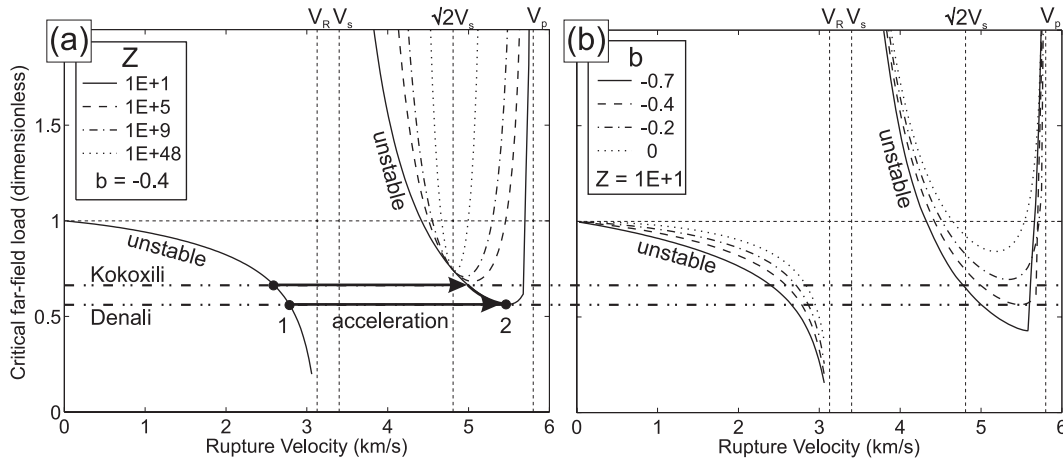


**Figure 12.** Rupture speed in the upper crust as a function of critical far-field load for a dynamically propagating mode II crack with a slip rate weakening cohesive zone and an imposed critical crack tip sliding-displacement criterion (equations from *Rosakis* [2002] and *Samudrala et al.* [2002]). The rupture speed stability curves are shown as a function of the (a) shear strength parameter  $Z$  and (b) slip rate weakening parameter  $\beta$ . For comparison, we plot our interpretations on the basis of the back projection results for the Kokoxili and Denali fault earthquakes, which indicate a transition from subshear to supershear speeds close to  $V_p$ .

(where the solution with no cohesive zone applies) normalized by the critical far-field shear stress required for quasi-static crack propagation  $(\sigma^D)^c \text{ dyn}/(\sigma^D)^c 0$ . The variation of the shear strength parameter of the pre-slip interface

$$Z = (\tau_0 D) / (\mu \delta_i^c) \quad (1)$$

where  $\tau_0$  is the bond strength (shear strength of the crack plane),  $\mu$  is the shear modulus, and  $\delta_i^c$  is the critical crack tip sliding displacement (breakdown slip), is graphed in Figure 12a. Curves with negative slopes represent unstable conditions; a rupture is likely to accelerate to higher speeds because propagation at those speeds requires less available energy to sustain the rupture (sometimes called “fracture energy,” “surface energy,” or “breakdown work”). Specifically, for a critical stress ratio less than 1 ( $y$  axis), the initial rupture speed is subshear and unstable. If there is an instability along the fault plane (e.g., variation in pre-slip stress or strength), the rupture can accelerate to stability at  $V_R$ . If the critical stress ratio intersects one of the curves in the supershear domain, the acceleration can jump past the forbidden region (between  $V_R$  and  $V_s$ , where propagation is physically unrealistic based on energy considerations [Broberg, 1964]) to a supershear speed, and accelerate under additional instabilities to the speed corresponding to the minimum between  $\sqrt{2} V_s$  and  $V_p$ . If the critical stress ratio is greater than 1, the rupture will initiate “spontaneously” at an unstable supershear speed between  $V_s$  and  $\sqrt{2} V_s$ , and if perturbed, can also accelerate to the stable minimum.

[59] This cohesive zone theory predicts that stable supershear rupture speed will vary as a function of both  $Z$ , the strength parameter, and  $\beta$ , the slip rate weakening parameter. This is shown by the shifts in the minima locations for the curves plotted in Figures 12a and 12b. Regardless of how the supershear rupture begins, faults with relatively large  $Z$  (strong faults, faults with low breakdown slips, or

low rigidity) promote rupture speeds closer to  $\sqrt{2} V_s$ , whereas faults with smaller  $Z$  may yield stable rupture speeds closer to  $V_p$ . The strength parameter  $Z$  does not influence the rupture speed for subshear speeds. The slip rate weakening parameter  $\beta$  influences the stable rupture speed regimes for both the subshear and supershear cases (Figure 12b). Greater velocity weakening (smaller  $\beta$ ) is associated with greater instability for both domains. For low- $Z$  faults in the supershear domain,  $\beta \leq -0.4$  promotes rupture speeds near  $V_p$ . For high- $Z$  faults in the supershear domain, the value of  $\beta$  only marginally influences the stability regime centered on  $\sqrt{2} V_s$ . As mentioned earlier, the above stability results have also been found by *Burridge et al.* [1979] and *Freund* [1979] using a slip-weakening law.

[60] In the bonded Homalite experiments, *Rosakis et al.* [1999] obtained a stable rupture just above  $\sqrt{2} V_s$  and estimated  $\beta = -0.4$ . They used a ratio of shear modulus to bond strength of 136, which corresponds to an exceptionally strong fault strength of 200 MPa in an equivalent crustal fault system [Rosakis, 2002]. Consequently, for crustal earthquakes, stable rupture speeds close to the crustal P wave speed suggest both a weaker fault and a slip rate weakening parameter  $\beta \leq -0.4$ .

[61] Our estimated Kokoxili and Denali supershear rupture speeds (5.7 and 5.5 km/s) do not rule out  $\sqrt{2} V_s$  speeds (i.e., 4.7 to 4.8 km/s; see resolution discussions above), but they correlate well with  $V_p$ , suggesting that the ruptures occurred along fault segments with relatively small  $Z$  values (weak faults) and significant slip or slip rate weakening. This is consistent with the high ratio of radiated energy to seismic moment reported for both earthquakes (Kokoxili  $6 \times 10^{-5}$ , Denali  $4.5 \times 10^{-5}$ ) as well as scaling relations applied to well-defined global strike-slip ruptures [Ozacar and Beck, 2004; Antolik et al., 2004]. The fracture energy per unit area (energy absorbed by the crack tip to allow the rupture to advance, sometimes referred to as “surface energy” or “breakdown work”) has been estimated for the

Kokoxili and Denali ruptures as 0.2–9.4 and 10–20 MJ/m<sup>2</sup> [Antolik *et al.*, 2004]. The low fracture energy for the Kokoxili rupture may be consistent with high rupture speeds, but some recent estimates of fracture energy for several M 5.6–7.2 earthquakes with presumably subshear rupture speeds yielded a wide range of fracture energies between 0.4 and 20 MJ/m<sup>2</sup> [Tinti *et al.*, 2005].

[62] The discussion above is mostly in the context of the theoretical, numerical, and laboratory results using an approach by Samudrala *et al.* [2002] and Rosakis [2002]. A more common approach involves the  $S$  parameter, introduced by Hamano [1974], defined as

$$S = \frac{\tau_s - \tau_1}{\tau_1 - \tau_d},$$

where  $\tau_s$  is the critical static frictional shear stress,  $\tau_d$  is the dynamic frictional shear stress (due to weakening), and  $\tau_1$  is the preslip stress on the fault. The numerator is the stress increase required to initiate slip and the denominator is the stress drop. Burridge [1973] analytically determined for 2-D unbounded cracks that  $S = 1.63$  is a critical value beneath which a slip-weakening rupture will accelerate from sub-Rayleigh to supershear speeds as the crack length grows. This value was later corrected to 1.77 [Andrews, 1985]. Dunham [2007] performed the same analysis for a 3-D unbounded elliptical crack and found a critical value of  $S = 1.19$ . Higher values of  $S$  will always lead to an initial sub-Rayleigh rupture speed that accelerates to  $V_R$  as the crack grows. Higher values of the critical stress ratio ( $y$  axis in Figure 12a) lead to smaller  $S$  values (Figure 12a); however, the exact relationship between the two is undefined because the semi-infinite crack in the Samudrala *et al.* [2002] model undergoes no stress drop as the stress across the crack is equal to that infinitely far ahead of the rupture (E. Dunham, personal communication, 2008). However, both ruptures extended to the surface. Recent work has shown that a strike-slip rupture bounded by a free surface can initiate, at the surface, a secondary rupture front that propagates at a near-sonic rupture speed [Chen and Zhang, 2006; Zhang and Chen, 2006]. Chen and Zhang [2006] and Zhang and Chen [2006] performed a number of 3-D numerical rupture experiments by extending the boundary integral equation method to a half-space model and found that the critical value of  $S$  can be as small as 1.0 for such strike-slip ruptures. Therefore, our imaging results suggest that  $S \leq 1.0$  for the main parts of both ruptures.

[63] Madariaga and Olsen [2000] numerically investigated the rupture process in the context of the parameter

$$\kappa = \frac{\tau_1^2 W}{\tau_s \mu D_c},$$

where for our purposes,  $W$  is the half depth of the fault,  $D_c$  is the critical slip-weakening distance, and the other parameters are defined above. Dunham [2007] has expressed  $\kappa$  in terms of  $S$  as

$$\kappa = 0.8(1 + S)^2 / l(S),$$

where  $l(S)$  is the ratio of the friction length (a length scale that depends on the friction law parameters governing the

nucleation process) to the transition length (the length the subshear rupture must propagate before transitioning to a supershear rupture speed). Madariaga and Olsen [2000] report that depending on the fault model type, the critical value of  $\kappa$  is 0.7 to 0.8. For smaller values, the rupture promptly arrests. Slightly larger values lead to rupture speed acceleration to  $V_R$ . For even larger values, the rupture starts at sub-Rayleigh speeds and accelerates to supershear speeds. The imaging results suggest that  $\kappa \geq 0.9$  for the main parts of the ruptures.

#### 4.4. Transition Zones

[64] The Kokoxili rupture transitioned from 2.6 to 5.7 km/s over a distance no greater than  $\sim 40$  km just east of the Hong Shui River gorge (Figures 3, 5, and 12), which also marks a change in the surface slip distribution from simple in the west to complex in the east for 70 km, past Kusai Hu Lake, to the junction point with the Kunlun Pass fault [Klinger *et al.*, 2005; Li *et al.*, 2005]. This complexity may be associated with the supershear rupture, since supershear propagation is associated with localized, amplified shear stresses just ahead of the rupture tip and possibly the opening of mode I cracks subparallel to the fault [e.g., Rosakis, 2002; Bhat *et al.*, 2007].

[65] From our images, we also estimate that the Denali rupture transitioned from 3.3 km/s to 5.5 km/s over a distance of no greater than  $\sim 40$  km. This transition begins at the intersection of the McKinley and main strand of the Denali fault system. This is also the location of strong motion station PS10, the station for which Ellsworth *et al.* [2004] and Dunham and Archuleta [2004] analyzed and modeled anomalously high-amplitude fault-perpendicular and fault-normal motions, suggesting that an asperity of higher initial shear stress, with a minimum width of 35 km, propelled the rupture from  $\sim 2.2$  to  $\sim 5.4$  km/s beginning about 30 km before PS10.

[66] It has recently been proposed on the basis of laboratory experiments of rupture dynamics that the length of transition from subshear to supershear speeds is on the order of tens of kilometers for crustal earthquakes [Xia *et al.*, 2004]. Our results suggest that the transition for both ruptures occurred over a length no longer than  $\sim 40$  km. This is also generally consistent with the results of Bouchon and Vallée [2003] and Robinson *et al.* [2006].

[67] Numerical modeling results of Andrews [1976] show that there is a gradual reduction in the width of the rupture front as the rupture prepares to transition from subshear to supershear speeds. This may explain why for both the Kokoxili and Denali ruptures, we do not image well the rupture just before the transition zone. Andrews' results also show that the rupture front has two branches during the transition, creating an effective rupture front that is much wider, and that following the transition, the supershear rupture front that remains also becomes gradually narrower with time. These qualitative predictions are also consistent with our imaging results.

#### 4.5. Comparisons and Speculations on the Rupture Process

[68] The kinematics of the Kokoxili and Denali fault earthquake ruptures are similar. Both ruptures were triggered by smaller ruptures on adjacent faults, initial rupture speeds

were stable and close to the Rayleigh wave speed, and a transition occurred to supershear speeds near the local P wave speeds.

[69] *Robinson et al.* [2006] and *Das* [2007] hypothesized that supershear rupture speeds may require relatively straight faults. The supershear segment that we image along the Kokoxili rupture occurred along a straight fault (similar to the results of Robinson et al.). The supershear segments of the Denali rupture also occurred along relatively straight faults, assuming the Denali and Totschunda faults are considered separately.

[70] It is interesting to speculate why these ruptures occurred. Rather than nucleate somewhere on the very long fault planes that ruptured, the events were triggered by failure on a neighboring fault. One can speculate that if there was great heterogeneity in prestress or strength along the ruptures, different patches of the faults would have ruptured at different times, prohibiting the buildup of stress that enabled the long ruptures to propagate at supershear speeds. As discussed above, our images also show rupture characteristics that appear similar to those obtained by numerical models that generally assume homogeneous stress and strength along generic faults [e.g., *Andrews*, 1976]. The shear stress on the Kokoxili and Denali faults was not so high that the faults ruptured spontaneously at supershear speeds, but rather at a critical speed that supported dynamic growth and transition to supershear speeds (Figure 12). Therefore, a very long fault that extends to the surface and has general homogeneity in prestress and fault strength, together with smaller adjacent fault segments to provide triggering, may be necessary ingredients to observe a sub-Rayleigh to supershear rupture transition in strike-slip earthquakes.

## 5. Conclusion

[71] Global back projection imaging of the teleseismic P wave train illuminates a transition in rupture speed from subshear to supershear speeds ( $\sim 5.6$  km/s) that approach the local P wave speed for the Kokoxili and Denali fault earthquakes. The transition occurs over a distance no greater than  $\sim 40$  km, which is consistent with an order-of-magnitude estimate based on recent lab experiments. The transitions begin after  $\sim 100$  km, and supershear persists for at least 200 km thereafter. Synthetic tests and other experiments with different frequency bands and imaging parameters suggest that our results are robust in that we can rule out subshear speeds along the imaged supershear segments. However, we cannot exclude supershear speeds within the range 4.5 to 6.5 km/s.

[72] The Kokoxili and Denali fault earthquakes produced perhaps the longest intracontinental strike-slip ruptures in modern seismic recording history, reaching rupture lengths of 340 to 400 km and maximum slips of at least 8 to 9 m. The rupture speed is a critical parameter for understanding the physics and evolution of the rupture process. Theoretical, numerical, and laboratory experiments show that rupture speeds approaching the P wave speed and the transition from subshear to supershear rupture speeds are physically possible. The most reliable, stable supershear rupture speeds that we image are remarkably similar, and close to the local P wave speed. This may suggest that these

intracontinental faults are generally weak, or have a high breakdown slip or crustal rigidity. Regardless, it appears that the faults exhibited at least moderate slip or slip rate weakening, and that relatively little work was required to sustain the supershear ruptures for long durations. That both faults are similar in these regards is interesting given that they have remarkably different geologic ages and slip histories. Previous published results and our observations lead us to speculate that very long strike-slip faults that extend to the surface and have general homogeneity in prestress and fault strength, together with smaller adjacent fault segments to provide triggering, may have been the necessary ingredients that permitted the sub-Rayleigh to supershear rupture speed transition to occur for both the Kokoxili and Denali ruptures.

[73] **Acknowledgments.** We thank Mike Taylor and Jeff Freymueller for fault location data for the Tibet and Alaska areas, respectively. We also thank Sigrun Hreinsdóttir for her Denali slip model and Michael Antolik for his preferred Kokoxili slip model. We thank Paul Earle for helpful feedback and organizing Denali waveform data during the initial part of this study and Christine Houser for her database of teleseismic P wave time shift corrections. We also thank Eric Dunham and Shamita Das for discussions that helped improve the manuscript and Alex Hutko, Nelson Pulido, and Eric Dunham for constructive reviews. Waveforms used in this study were downloaded from the IRIS Data Management Center. We thank the National Science Foundation and the USGS NEHRP program for funding this research.

## References

- Allmann, B. P., and P. M. Shearer (2007), A high-frequency secondary event during the 2004 Parkfield earthquake, *Science*, *318*, 1279–1283, doi:10.1126/science.1146537.
- Andrews, D. (1976), Rupture velocity of plane strain shear cracks, *J. Geophys. Res.*, *81*(32), 5679–5687, doi:10.1029/JB081i032p05679.
- Andrews, D. (1985), Dynamic plane-strain shear rupture with a slip-weakening friction law calculated by a boundary integral method, *Bull. Seismol. Soc. Am.*, *75*, 1–21.
- Antolik, M., R. E. Abercrombie, and G. Ekstrom (2004), The 14 November 2001 Kokoxili (Kunlunshan), Tibet, earthquake: Rupture transfer through a large extensional step-over, *Bull. Seismol. Soc. Am.*, *94*, 1173–1194, doi:10.1785/012003180.
- Archuleta, R. (1984), A faulting model for the 1979 Imperial Valley earthquake, *J. Geophys. Res.*, *89*, 4559–4585, doi:10.1029/JB089iB06p04559.
- Asano, K., T. Iwata, and K. Irikura (2005), Estimation of source rupture process and strong ground motion simulation of the 2002 Denali, Alaska, earthquake, *Bull. Seismol. Soc. Am.*, *95*, 1701–1715, doi:10.1785/0120040154.
- Baysal, E., D. D. Kosloff, and J. W. C. Sherwood (1983), Reverse time migration, *Geophysics*, *48*, 1514–1524, doi:10.1190/1.1441434.
- Beresnev, I. (2003), Uncertainties in finite-fault slip inversions: To what extent to believe? (a critical review), *Bull. Seismol. Soc. Am.*, *93*, 2445–2458, doi:10.1785/0120020225.
- Bhat, H. S., R. Dmowska, G. C. P. King, Y. Klinger, and J. R. Rice (2007), Off-fault damage patterns due to supershear ruptures with application to the 2001  $M_w$  8.1 Kokoxili (Kunlun) Tibet earthquake, *J. Geophys. Res.*, *112*, B06301, doi:10.1029/2006JB004425.
- Bleistein, N. (1987), On the imaging of reflectors in the Earth, *Geophysics*, *52*, 931–942, doi:10.1190/1.1442363.
- Bouchon, M., and M. Vallée (2003), Observation of long supershear rupture during the magnitude 8.1 Kunlunshan earthquake, *Science*, *301*, 824–826, doi:10.1126/science.1086832.
- Bouchon, M., N. Toksoz, H. Karabulut, M.-P. Bouin, M. Dietrich, M. Aktar, and M. Edie (2000), Seismic imaging of the 1999 Izmit (Turkey) rupture inferred from the near-fault recordings, *Geophys. Res. Lett.*, *27*, 3013–3016, doi:10.1029/2000GL011761.
- Bouchon, M., M.-P. Bouin, H. Karabulut, M. Toksoz, M. Dietrich, and A. Rosakis (2001), How fast is rupture during an earthquake? New insights from the 1999 Turkey earthquakes, *Geophys. Res. Lett.*, *28*, 2723–2726, doi:10.1029/2001GL013112.
- Broberg, K. B. (1964), On the speed of a brittle crack, *J. Appl. Mech.*, *31*, 546–547.
- Brocher, T. M., G. S. Fuis, W. J. Lutter, N. I. Christensen, and N. A. Ratchkovski (2004), Seismic velocity models for the Denali fault zone

- along the Richardson highway, Alaska, *Bull. Seismol. Soc. Am.*, *94*, S85–S106, doi:10.1785/0120040615.
- Burridge, R. (1973), Admissible speeds for plane-strain self-similar shear cracks with friction but lacking cohesion, *Geophys. J. R. Astron. Soc.*, *35*, 439–455.
- Burridge, R., G. Conn, and L. B. Freund (1979), The stability of a rapid mode II shear crack with cohesive traction, *J. Geophys. Res.*, *84*, 2210–2221, doi:10.1029/JB084iB05p02210.
- Chen, L., J. R. Booker, A. G. Jones, N. Wu, M. J. Unsworth, W. Wei, and H. Tan (1996), Electrically conductive crust in southern Tibet from INDEPTH magnetotelluric surveying, *Science*, *274*, 1694–1696, doi:10.1126/science.274.5293.1694.
- Chen, X., and H. Zhang (2006), Modelling rupture dynamics of a planar fault in 3-D half space by boundary integral equation method: An overview, *Pure Appl. Geophys.*, *163*, 267–299, doi:10.1007/s00024-005-0020-z.
- Chun, K.-Y., and T. Yoshii (1977), Crustal structure of the Tibetan Plateau: A surface-wave study by a moving window analysis, *Bull. Seismol. Soc. Am.*, *67*, 735–750.
- Claerbout, J. F. (1971), Toward a unified theory of reflector mapping, *Geophysics*, *36*, 467–481, doi:10.1190/1.1440185.
- Crone, A. J., S. F. Personius, P. A. Craw, P. J. Haeussler, and L. A. Staft (2004), The Susitna Glacier thrust fault: Characteristics of surface ruptures on the fault that initiated the 2002 Denali fault earthquake, *Bull. Seismol. Soc. Am.*, *94*, S5–S22, doi:10.1785/0120040619.
- Das, S. (2007), The need to study speed, *Science*, *317*, 905–906, doi:10.1126/science.1142143.
- Das, S., and K. Aki (1977), A numerical study of two-dimensional spontaneous rupture propagation, *Geophys. J. R. Astron. Soc.*, *50*, 643–668.
- Day, S. M. (1982), Three-dimensional simulation of spontaneous rupture: The effect of non-uniform prestress, *Bull. Seismol. Soc. Am.*, *72*, 1851–1902.
- Dreger, D. S., D. D. Oglesby, R. Harris, N. Ratchkovski, and R. Hansen (2004), Kinematic and dynamic rupture models of the November 3, 2002  $M_w$  7.9 Denali, Alaska, earthquake, *Geophys. Res. Lett.*, *31*, L04605, doi:10.1029/2003GL018333.
- Dunham, E. M. (2007), Conditions governing the occurrence of supershear ruptures under slip-weakening friction, *J. Geophys. Res.*, *112*, B07302, doi:10.1029/2006JB004717.
- Dunham, E. M., and R. J. Archuleta (2004), Evidence for a supershear transient during the 2002 Denali fault earthquake, *Bull. Seismol. Soc. Am.*, *94*(6B), S256–S268, doi:10.1785/0120040616.
- Dunham, E. M., P. Favreau, and J. M. Carlson (2003), A supershear transition mechanism for cracks, *Science*, *299*, 1557–1559, doi:10.1126/science.1080650.
- Earle, P. S., and P. M. Shearer (1994), Characterization of global seismograms using an automatic-picking algorithm, *Bull. Seismol. Soc. Am.*, *84*, 366–376.
- Eberhart-Phillips, D., et al. (2003), The 2002 Denali fault earthquake, Alaska: A large magnitude, slip-partitioned event, *Science*, *300*, 1113–1118, doi:10.1126/science.1082703.
- Ellsworth, W. L., M. Celebi, J. R. Evans, E. G. Jensen, R. Kayen, M. C. Metz, D. J. Nyman, J. W. Roddick, P. Spudich, and C. D. Stephens (2004), Near-field ground motion of the 2002 Denali fault, Alaska, earthquake recorded at pump station 10, *Earthquake Spectra*, *20*, 597–615, doi:10.1193/1.1778172.
- Ferris, A., G. A. Abers, D. H. Christensen, and E. Veenstra (2003), High-resolution image of the subducted Pacific (?) plate beneath central Alaska, 50–150 km depth, *Earth Planet. Sci. Lett.*, *214*, 575–588, doi:10.1016/S0012-821X(03)00403-5.
- Frankel, A. (2004), Rupture process of the M 7.9 Denali fault, Alaska, earthquake: Subevents, directivity, and scaling of high-frequency ground motions, *Bull. Seismol. Soc. Am.*, *94*(6B), S234–S255, doi:10.1785/0120040612.
- Freund, L. B. (1979), The mechanics of dynamic shear crack propagation, *J. Geophys. Res.*, *84*, 2199–2209, doi:10.1029/JB084iB05p02199.
- Haeussler, P. J., et al. (2004), Surface rupture and slip distribution of the Denali and Totschunda faults in the 3 November 2002 M 7.9 earthquake, Alaska, *Bull. Seismol. Soc. Am.*, *94*, S23–S52, doi:10.1785/0120040626.
- Hamano, Y. (1974), Dependence of rupture time history on the heterogeneous distribution of stress and strength on the fault (abstract), *Eos Trans. AGU*, *55*, 352.
- Hartzell, S. H., and T. H. Heaton (1983), Inversion of strong ground motion and teleseismic waveform data for the fault rupture history of the 1979 Imperial Valley, California, earthquake, *Bull. Seismol. Soc. Am.*, *73*, 1553–1583.
- Hernandez, B., F. Cotton, and M. Campillo (1999), Contribution of radar interferometry to a two-step inversion of the kinematic process of the 1992 Landers earthquake, *J. Geophys. Res.*, *104*, 13,083–13,099, doi:10.1029/1999JB900078.
- Hirn, A., et al. (1984), Crustal structure and variability of the Himalayan border of Tibet, *Nature*, *307*, 25–27, doi:10.1038/307025a0.
- Houser, C., G. Masters, P. Shearer, and G. Laske (2008), Shear and compressional velocity models of the mantle from cluster analysis of long-period waveforms, *Geophys. J. Int.*, *174*, 195–212, doi:10.1111/j.1365-246X.2008.03763.x.
- Hreinsdóttir, S., J. T. Freymueller, R. Bürgmann, and J. Mitchell (2006), Coseismic deformation of the 2002 Denali fault earthquake: Insights from GPS measurements, *J. Geophys. Res.*, *111*, B03308, doi:10.1029/2005JB003676.
- Ishii, M., P. M. Shearer, H. Houston, and J. E. Vidale (2005), Extent, duration and speed of the 2004 Sumatra-Andaman earthquake imaged by the Hi-net array, *Nature*, *435*, 933–936, doi:10.1038/nature03675.
- Ishii, M., P. M. Shearer, H. Houston, and J. E. Vidale (2007), Teleseismic P wave imaging of the 26 December 2004 Sumatra-Andaman and 28 March 2005 Sumatra earthquake ruptures using the Hi-net array, *J. Geophys. Res.*, *112*, B11307, doi:10.1029/2006JB004700.
- Jin, D. J., and E. Herrin (1980), Surface wave studies of the Bering Sea and Alaska area, *Bull. Seismol. Soc. Am.*, *70*, 2117–2144.
- Kao, H., and S.-J. Shan (2004), The source-scanning algorithm: Mapping the distribution of seismic sources in time and space, *Geophys. J. Int.*, *157*, 589–594, doi:10.1111/j.1365-246X.2004.02276.x.
- Kao, H., and S.-J. Shan (2007), Rapid identification of earthquake rupture plane using source-scanning algorithms, *Geophys. J. Int.*, *168*, 1011–1020, doi:10.1111/j.1365-246X.2006.03271.x.
- Kao, H., K. Wang, R. Chen, I. Wada, J. He, and S. Malone (2008), Identifying the rupture plane of the 2001 Nisqually, Washington, earthquake, *Bull. Seismol. Soc. Am.*, *98*, 1546–1558, doi:10.1785/0120070160.
- Kato, N., and T. Hirasawa (1996), Effects of strain rate and strength non-uniformity on the slip nucleation process: A numerical experiment, *Tectonophysics*, *265*, 299–311, doi:10.1016/S0040-1951(96)00089-3.
- Kennett, B. L. N., and E. R. Engdahl (1991), Traveltimes for global earthquake location and phase identification, *Geophys. J. Int.*, *105*, 429–465, doi:10.1111/j.1365-246X.1991.tb06724.x.
- Kikuchi, M., and H. Kanamori (1982), Inversion of complex body waves, *Bull. Seismol. Soc. Am.*, *72*, 491–506.
- Kilgore, B. D., M. L. Blanpied, and J. H. Dietrich (1993), Velocity dependent friction of granite over a wide range of conditions, *Geophys. Res. Lett.*, *20*, 903–906, doi:10.1029/93GL00368.
- Kind, R., J. Ni, W. Zhao, J. Wu, X. Yuan, L. Zhao, E. Sandvol, C. Reese, J. Nabelek, and T. Hearn (1996), Evidence from earthquake data for a partially molten crustal layer in southern Tibet, *Science*, *274*, 1692–1694, doi:10.1126/science.274.5293.1692.
- Klinger, Y., X. Xu, P. Tapponnier, J. Van der Woerd, C. Lasserre, and G. King (2005), High-resolution satellite imagery mapping of the surface rupture and slip distribution of the  $M_w$  7.8, 14 November 2001 Kokoxili earthquake, Kunlun fault, northern Tibet, China, *Bull. Seismol. Soc. Am.*, *95*, 1970–1987, doi:10.1785/0120040233.
- Krüger, F., and M. Ohrnberger (2005), Tracking the rupture of the  $M_w = 9.3$  Sumatra earthquake over 1,150 km at teleseismic distance, *Nature*, *435*, 937–939, doi:10.1038/nature03695.
- Lanphere, M. A. (1978), Displacement history of the Denali fault system, Alaska and Canada, *Can. J. Earth Sci.*, *15*, 817–822.
- Larmat, C., J.-P. Montagner, M. Fink, Y. Capdeville, A. Tourin, and E. Clevede (2006), Time-reversal imaging of seismic sources and application to the great Sumatra earthquake, *Geophys. Res. Lett.*, *33*, L19312, doi:10.1029/2006GL026336.
- Li, H., J. Van der Woerd, P. Tapponnier, Y. Klinger, X. Qi, J. Yang, and Y. Zhu (2005), Slip rate on the Kunlun Fault at Hongshui Gou, and recurrence time of great events comparable to the 14/11/2001,  $M_w$  7.9 Kokoxili earthquake, *Earth Planet. Sci. Lett.*, *237*, 285–299, doi:10.1016/j.epsl.2005.05.041.
- Liao, B.-Y., and H.-C. Huang (2008), Rupture process of the 2002  $M_w$  7.9 Denali earthquake, Alaska, using a newly devised hybrid blind deconvolution method, *Bull. Seismol. Soc. Am.*, *98*, 162–179, doi:10.1785/0120050065.
- Lin, A., B. Fu, J. Guo, Q. Zeng, G. Dang, W. He, and Y. Zhao (2002), Coseismic strike-slip and rupture length produced by the 2001  $M_s$  8.1 central Kunlun earthquake, *Science*, *296*, 2015–2017, doi:10.1126/science.1070879.
- Lin, A., M. Kikuchi, and B. Fu (2003), Rupture segmentation and process of the 2001  $M_w$  7.8 central Kunlun, China, earthquake, *Bull. Seismol. Soc. Am.*, *93*, 2477–2492, doi:10.1785/0120020179.
- Madariaga, R., and K. B. Olsen (2000), Criticality of rupture dynamics in 3D, *Pure Appl. Geophys.*, *157*, 1981–2001, doi:10.1007/PL00001071.
- Makovsky, Y., and S. L. Klemperer (1999), Measuring the seismic properties of Tibetan bright spots: Evidence for free aqueous fluids in the Tibetan middle crust, *J. Geophys. Res.*, *104*, 10,795–10,825, doi:10.1029/1998JB900074.

- Makovsky, Y., S. Klemperer, L. Ratschbacher, L. D. Brown, M. Li, W. Zhao, and F. Meng (1996), INDEPTH wide-angle reflection observation of P-wave-to-S-wave conversion from crustal bright spots in Tibet, *Science*, *274*, 1690–1691, doi:10.1126/science.274.5293.1690.
- McMechan, G. A. (1983), Migration by extrapolation of time-dependent boundary values, *Geophys. Prospect.*, *31*, 413–420, doi:10.1111/j.1365-2478.1983.tb01060.x.
- Meyer, B., P. Tapponnier, L. Bourjot, F. Metivier, Y. Gaudemer, G. Peltzer, G. Shunmin, and C. Zhitai (1998), Crustal thickening in Gansu-Qinghai, lithospheric mantle subduction, and oblique, strike-slip controlled growth of the Tibet plateau, *Geophys. J. Int.*, *135*, 1–47, doi:10.1046/j.1365-246X.1998.00567.x.
- Miller, T. P. (1994), Geothermal resources of Alaska, in *The Geology of North America*, vol. G-1, *Geology of Alaska*, pp. 979–987, Geol. Soc. of Am., Boulder, Colo.
- Nelson, K. D., et al. (1996), Partially molten middle crust beneath southern Tibet: Synthesis of project INDEPTH results, *Science*, *274*, 1684–1688, doi:10.1126/science.274.5293.1684.
- Nokleberg, W. J., G. Plafker, and F. H. Wilson (1994), Geology of south-central Alaska, in *The Geology of North America*, vol. G-1, *Geology of Alaska*, pp. 311–366, Geol. Soc. of Am., Boulder, Colo.
- Olsen, A. H., and R. J. Apse (1982), Finite faults and inverse theory with applications to the 1979 Imperial Valley earthquake, *Bull. Seismol. Soc. Am.*, *72*, 1969–2001.
- Olsen, K. B., R. Madariaga, and R. J. Archuleta (1997), Three-dimensional dynamic simulation of the 1992 Landers earthquake, *Science*, *278*, 834–838, doi:10.1126/science.278.5339.834.
- Olson, J. V., C. R. Wilson, and R. A. Hansen (2003), Infrasound associated with the 2002 Denali fault earthquake, Alaska, *Geophys. Res. Lett.*, *30*(23), 2195, doi:10.1029/2003GL018568.
- Ozacar, A. A., and S. L. Beck (2004), The 2002 Denali fault and 2001 Kunlun fault earthquakes: Complex rupture process of two large strike-slip events, *Bull. Seismol. Soc. Am.*, *94*, S278–S292, doi:10.1785/0120040604.
- Peltzer, G., and F. Saucier (1996), Present-day kinematics of Asia derived from geologic fault rates, *J. Geophys. Res.*, *101*, 27,943–27,956, doi:10.1029/96JB02698.
- Plafker, G., and H. C. Berg (1994), Overview of the geology and tectonics evolution of Alaska, in *The Geology of North America*, vol. G-1, *Geology of Alaska*, pp. 989–1021, Geol. Soc. of Am., Boulder, Colo.
- Plafker, G., L. Gilpin, and J. C. Lahr (1994), Neotectonic map of Alaska, in *The Geology of North America*, vol. G-1, *Geology of Alaska*, plate 12, Geol. Soc. of Am., Boulder, Colo.
- Rice, J. R., and A. Ruina (1983), Stability of steady frictional slipping, *J. Appl. Mech.*, *50*, 343–349.
- Robinson, D. P., C. Brough, and S. Das (2006), The  $M_w$  7.8 2001 Kunlunshan earthquake: Extreme rupture speed variability and effect on fault geometry, *J. Geophys. Res.*, *111*, B08303, doi:10.1029/2005JB004137.
- Rosakis, A. J. (2002), Intersonic shear cracks and fault ruptures, *Adv. Phys.*, *51*, 1189–1257, doi:10.1080/00018730210122328.
- Rosakis, A. J., O. Samudrala, and D. Coker (1999), Cracks faster than the shear wave speed, *Science*, *284*, 1337–1340, doi:10.1126/science.284.5418.1337.
- Rossi, G., G. A. Abers, S. Rondenay, and D. H. Christensen (2006), Unusual mantle Poisson's ratio, subduction and crustal structure in Central Alaska, *J. Geophys. Res.*, *111*, B09311, doi:10.1029/2005JB003956.
- Ruina, A. (1983), Slip instability and state variable friction laws, *J. Geophys. Res.*, *88*, 10,359–10,370, doi:10.1029/JB088iB12p10359.
- Samudrala, O., Y. Huang, and A. J. Rosakis (2002), Subsonic and intersonic shear rupture of weak planes with a velocity weakening cohesive zone, *J. Geophys. Res.*, *107*(B8), 2170, doi:10.1029/2001JB000460.
- Sekiguchi, H., and T. Iwata (2002), Rupture process of the 1999 Kocaeli, Turkey, earthquake estimated from strong-motion waveforms, *Bull. Seismol. Soc. Am.*, *92*, 300–311, doi:10.1785/0120000811.
- Shao, G., and C. Ji (2007), The rupture velocity of the 2001 Kunlunshan earthquake: A revisit (abstract), *Eos Trans. AGU*, *88*(52), Fall Meeting Suppl., Abstract S51B–0513.
- Spudich, P., and E. Cranswick (1984), Direct observation of rupture propagation during the 1979 Imperial Valley earthquake using a short baseline accelerometer array, *Bull. Seismol. Soc. Am.*, *79*, 2083–2114.
- Stolt, R. H. (1978), Migration by Fourier transform, *Geophysics*, *43*, 23–48, doi:10.1190/1.1440826.
- Sun, Y., F. Qin, S. Checkles, and J. Leveille (2000), 3-D prestack Kirchhoff beam migration for depth imaging, *Geophysics*, *65*, 1592–1603, doi:10.1190/1.1444847.
- Tapponnier, P., Z. Q. Xu, F. Roger, B. Meyer, N. Arnaud, G. Wittlinger, and J. S. Yang (2001), Oblique stepwise rise and growth of the Tibet Plateau, *Science*, *294*, 1671–1677, doi:10.1126/science.105978.
- Tinti, E., E. Fukuyama, A. Piatanesi, and M. Cocco (2005), Kinematic source-time function compatible with earthquake dynamics, *Bull. Seismol. Soc. Am.*, *95*, 1211–1223.
- Vallée, M., M. Landès, N. M. Shapiro, and Y. Klinger (2008), The 14 November 2001 Kokoxili (Tibet) earthquake: High-frequency seismic radiation originating from the transitions between sub-Rayleigh and supershear rupture velocity regimes, *J. Geophys. Res.*, *113*, B07305, doi:10.1029/2007JB005520.
- Van der Woerd, J., F. J. Ryerson, P. Tapponnier, Y. Gaudemer, R. Finkel, A.-S. Meriaux, M. W. Caffee, Z. Guoguang, and H. Qunlu (1998), Holocene left-slip rate determined by cosmogenic surface dating on the Xidatan segment of the Kunlun fault, *Geology*, *26*, 695–698, doi:10.1130/0091-7613(1998)026<0695:HLSRDB>2.3.CO;2.
- Van der Woerd, J., F. J. Ryerson, P. Tapponnier, A.-S. Meriaux, Y. Gaudemer, B. Meyer, R. C. Finkel, M. W. Caffee, Z. Guoguang, and X. Zhiqin (2000), Uniform slip-rate along the Kunlun fault: Implications for seismic behaviour and large-scale tectonics, *Geophys. Res. Lett.*, *27*, 2353–2356, doi:10.1029/1999GL011292.
- Van der Woerd, J., P. Tapponnier, F. J. Ryerson, A.-S. Meriaux, B. Meyer, Y. Gaudemer, R. C. Finkel, M. W. Caffee, Z. Guoguang, and X. Zhiqin (2002), Uniform postglacial slip-rate along the central 600 km of the Kunlun Fault (Tibet), from  $^{26}\text{Al}$ ,  $^{10}\text{Be}$ , and  $^{14}\text{C}$  dating of riser offsets, and climatic origin of the regional morphology, *Geophys. J. Int.*, *148*, 356–388, doi:10.1046/j.1365-246x.2002.01556.x.
- Walker, K. T., M. Ishii, and P. M. Shearer (2005), Rupture details of the 28 March 2005 Sumatra  $M_w$  8.6 earthquake imaged with teleseismic P waves, *Geophys. Res. Lett.*, *32*, L24303, doi:10.1029/2005GL024395.
- Xia, K., A. J. Rosakis, and H. Kanamori (2004), Laboratory earthquakes: The sub-Rayleigh-to-supershear rupture transition, *Science*, *303*, 1859–1861, doi:10.1126/science.1094022.
- Xu, X., W. Chen, W. Ma, G. Yu, and G. Chen (2002), Surface rupture of the Kunlunshan earthquake ( $M_s$  8.1), northern Tibetan Plateau, China, *Seismol. Res. Lett.*, *73*, 884–892.
- Zhang, H., and X. Chen (2006), Dynamic rupture on a planar fault in three-dimensional half-space—II. Validations and numerical experiments, *Geophys. J. Int.*, *167*, 917–932, doi:10.1111/j.1365-246X.2006.03102.x.
- Zhao, Z., and R.-S. Zeng (1993), The P and S wave velocity structures of the crust and upper mantle beneath Tibetan Plateau, *Acta Seismol. Sin.*, *6*, 299–304, doi:10.1007/BF02650942.

P. M. Shearer and K. T. Walker, Institute of Geophysics and Planetary Physics, Scripps Institution of Oceanography, University of California, San Diego, 9500 Gillman Avenue, MC 0225, La Jolla, CA 92093, USA. (walker@ucsd.edu)